Monthly Notices of the ROYAL ASTRONOMICAL SOCIETY

MNRAS **498,** 4150–4177 (2020) doi:10.1093/mnras/staa2413
Advance Access publication 2020 September 2

Ionized outflows in local luminous AGN: what are the real densities and outflow rates?

R. Davies [1]★ D. Baron,[2] T. Shimizu [1] H. Netzer,[2] L. Burtscher,[3] P. T. de Zeeuw,[1,3] R. Genzel,[1] E. K. S. Hicks,[4] M. Koss [5] M.-Y. Lin,[6] D. Lutz,[1] W. Maciejewski,[7] F. Müller-Sánchez,[8] G. Orban de Xivry,[9] C. Ricci,[10,11] R. Riffel [12] R. A. Riffel [13] D. Rosario,[14] M. Schartmann,[1] A. Schnorr-Müller,[12] J. Shangguan,[1] A. Sternberg,[2] E. Sturm,[1] T. Storchi-Bergmann,[12] L. Tacconi[1] and S. Veilleux[15]

[1]*Max-Planck-Institut für extraterrestrische Physik, Postfach 1312, D-85741 Garching, Germany*
[2]*School of Physics and Astronomy, Tel-Aviv University, Tel Aviv 69978, Israel*
[3]*Leiden Observatory, Leiden University, PO Box 9513, NL-2300 RA Leiden, the Netherlands*
[4]*Department of Physics and Astronomy, University of Alaska Anchorage, Anchorage, AK 99508-4664, USA*
[5]*Eureka Scientific, 2452 Delmer Street Suite 100, Oakland, CA 94602-3017, USA*
[6]*Institute of Astronomy and Astrophysics, Academia Sinica, Roosevelt Rd, Taipei 10617, Taiwan*
[7]*Astrophysics Research Institute, Liverpool John Moores University, IC2 Liverpool Science Park, 146 Brownlow Hill, Liverpool L3 5RF, UK*
[8]*Physics Department, University of Memphis, Memphis, TN 38152, USA*
[9]*Space Sciences, Technologies, and Astrophysics Research Institute, Université de Liège, B-4000 Sart Tilman, Belgium*
[10]*Núcleo de Astronomía de la Facultad de Ingeniería, Universidad Diego Portales, Av. Ejército Libertador 441, Santiago, Chile*
[11]*Kavli Institute for Astronomy and Astrophysics, Peking University, Beijing 100871, China*
[12]*Departamento de Astronomia, Universidade Federal do Rio Grande do Sul, IF, CP 15051, 91501-970 Porto Alegre, RS, Brazil*
[13]*Departamento de Física, Universidade Federal de Santa Maria, 97105-900 Santa Maria, RS, Brazil*
[14]*Department of Physics, Durham University, South Road, Durham DH1 3LE, UK*
[15]*Department of Astronomy and Joint Space-Science Institute, University of Maryland, College Park, MD 20742-2421, USA*

Accepted 2020 August 9. Received 2020 July 17; in original form 2020 March 12

ABSTRACT

We report on the determination of electron densities, and their impact on the outflow masses and rates, measured in the central few hundred parsecs of 11 local luminous active galaxies. We show that the peak of the integrated line emission in the active galactic nuclei (AGN) is significantly offset from the systemic velocity as traced by the stellar absorption features, indicating that the profiles are dominated by outflow. In contrast, matched inactive galaxies are characterized by a systemic peak and weaker outflow wing. We present three independent estimates of the electron density in these AGN, discussing the merits of the different methods. The electron density derived from the [S II] doublet is significantly lower than that found with a method developed in the last decade using auroral and transauroral lines, as well as a recently introduced method based on the ionization parameter. The reason is that, for gas photoionized by an AGN, much of the [S II] emission arises in an extended partially ionized zone where the implicit assumption that the electron density traces the hydrogen density is invalid. We propose ways to deal with this situation and we derive the associated outflow rates for ionized gas, which are in the range 0.001–0.5 $M_\odot$ yr^{-1} for our AGN sample. We compare these outflow rates to the relation between $\dot{M}_{\rm out}$ and $L_{\rm AGN}$ in the literature, and argue that it may need to be modified and rescaled towards lower mass outflow rates.

Key words: galaxies: active – galaxies: ISM – galaxies: nuclei – galaxies: Seyfert.

1 INTRODUCTION

The evidence that outflows, whether driven by star formation or active galactic nuclei (AGN), play a fundamental role in the evolution of galaxies is now long undisputed (Veilleux, Cecil & Bland-Hawthorn 2005) and numerous reviews have been written about different aspects of the subject. Some of the most striking evidence comes from observations of galaxy clusters, in which mechanical feedback from radio jets heats the intracluster medium (Fabian 2012). This is associated with the more massive black holes in classical bulges and elliptical galaxies. Large surveys have shown this appears to be distinct from radiative feedback that occurs at accretion rates above 1 per cent Eddington and is primarily associated with less massive black holes fed by secular process or minor mergers (Heckman & Best 2014). Through studies of ultrafast outflows, which have speeds in excess of $\sim$0.1c, a theoretical framework has been developed about the impact of the wind on the interstellar medium (ISM), and how its dependency on the bulge mass might lead to the observed relation between black hole mass and global properties of the stellar

★ E-mail: davies@mpe.mpg.de

bulge (King & Pounds 2015). A broader framework, encompassing cosmological models of galaxy evolution, highlights the role that outflows are expected to have in order for such models to reproduce the observed galaxy scaling relations (Somerville & Davé 2015). Through sensitive observations at millimetre wavelengths, it has been realized that cool outflows of neutral and molecular gas play perhaps an even more significant role than the ionized outflows (Veilleux et al. 2020). However, the amount of gas in each phase of the outflow, whether the outflow escapes the host galaxy, or if it has a significant impact on the global star formation rate, is not yet firmly established although some efforts have been made in this direction (Fiore et al. 2017; Morganti 2017).

As emphasized by Harrison et al. (2018), for ionized outflows, a large part of the uncertainty is directly linked to the density of gas in the outflow. The reason is straightforward to show because, at a fixed (i.e. the observed) line luminosity, the derived mass of ionized gas, and hence outflow rate, is inversely proportional to the adopted density. The line luminosity is $L_{\rm line} = \gamma_{\rm line}\, n_{\rm e}\, n_{\rm p}\, V f$, where $\gamma_{\rm line}$ is the appropriate volume emissivity, $n_{\rm e} \sim n_{\rm p}$ is the electron or equivalently ion density, V is the volume, and f the filling factor. An additional implicit assumption is that $n_{\rm e} \sim n_{\rm H}$, i.e. the clouds are fully ionized. In this case, the mass of ionized gas in that volume is $M_{\rm out} = \mu m_{\rm H}\, n_{\rm p}\, V f$, where $\mu m_{\rm H}$ is the effective atomic mass. Together these show that the dependencies of the derived ionized gas mass are $M_{\rm out} \propto L_{\rm line} / (\gamma_{\rm line}\, n_{\rm e})$ and equivalently the dependencies for the outflow rate are $\dot{M}_{\rm out} \propto L_{\rm line}\, v_{\rm out} / (\gamma_{\rm line}\, n_{\rm e}\, r_{\rm out})$. Thus, a reliable assessment of the density in the outflow, which is appropriate to the spatial scales being measured, is an essential ingredient for deriving the outflow mass and rate.

In the literature, a wide range of different densities (either assumed or measured), covering several orders of magnitude, have been used when deriving quantities related to ionized outflows driven by AGN. These include, at low and high redshift: 100 cm^{-3} (Liu et al. 2013; Riffel, Storchi-Bergmann & Winge 2013; Harrison et al. 2014; Kakkad et al. 2016; Rupke, Gültekin & Veilleux 2017); 200 cm^{-3} (Fiore et al. 2017); 500 cm^{-3} (Storchi-Bergmann et al. 2010; Carniani et al. 2015; Riffel, Storchi-Bergmann & Riffel 2015); 1000-1500 cm^{-3} (Schnorr-Müller et al. 2016a; Perna et al. 2017; Förster Schreiber et al. 2019; Shimizu et al. 2019); 5000 cm^{-3} (Müller-Sánchez et al. 2011); and in some instances densities of 10^4–10^5 cm^{-3} have been reported (Holt et al. 2011; Rose et al. 2018; Santoro et al. 2018; Baron & Netzer 2019). Among this plethora of values, lower densities are often adopted or measured for larger scales of 1–10 kpc, while the higher densities apply to smaller 0.1–1 kpc scales. This tendency is also reflected in spatially resolved studies (e.g. Baron et al. 2018; Freitas et al. 2018; Kakkad et al. 2018; do Nascimento et al. 2019; Hinkle, Veilleux & Rupke 2019; Shimizu et al. 2019) that tend to show that $n_{\rm e}$ decreases with radius.

In this paper, we make use of the high-quality spectroscopic data available for the Local Luminous AGN with Matched Analogues (LLAMA) survey (Davies et al. 2015) to derive electron densities in the outflowing gas. These are then used to estimate the outflow rates, which are compared to well-known relations between AGN luminosity and outflow rate. This paper begins with a description of the sample and observations in Section 2, together with estimates of the systemic velocity and a discussion of how the stellar continuum is subtracted. In Section 3, we argue, based on the line ratios and profiles, that the entire line profile in these AGN is dominated by outflow, and any systemic component is subdominant. Because of this, when deriving densities, we integrate over the complete emission lines. The outflow densities are derived using three independent methods, which are summarized in Section 4. They are the standard method of the [S II] λλ6716/6731 doublet ratio; a method developed by Holt et al. (2011) that makes use of auroral and transauroral lines in the ratios [S II] λλ(6716+6731)/[S II] λλ(4069+4076) and [O II] λλ(3726+3729)/[O II] λλ(7320+7331); and a method recently introduced by Baron & Netzer (2019) that is based on the definition of the ionization parameter. We discuss the merits of the various methods and present the densities derived from our sample of AGN for each of them. Using the density measure that we argue is most appropriate, in Section 5 we assess whether the derived outflow rates extend the lower luminosity end of the $L_{\rm AGN}$–$\dot{M}_{\rm out}$ relation proposed by Fiore et al. (2017). We finish with our conclusions in Section 6.

2 SAMPLE AND OBSERVATIONS

2.1 Sample

We make use of the LLAMA sample of active and inactive galaxies. Davies et al. (2015) provide the rationale for the sample, and a detailed description of its selection. The key aspect is that these are taken from the all-sky flux-limited 14–195 keV 58-month *Swift*-Burst Alert Telescope (BAT) survey (Baumgartner et al. 2013) in such a way as to create a volume-limited sample of active galaxies that is as unbiased as possible, for detailed study using optical spectroscopy and adaptive optics integral field near-infrared (NIR) spectroscopy. The sole selection criteria were $z < 0.01$ (corresponding to a distance of ∼40 Mpc), $\log L_{14-195\,\rm keV}$ [erg s^{-1}] > 42.5 (using redshift distance), and $\delta < 15^\circ$ so that they are observable from the Very Large Telescope (VLT). This yielded 20 AGN. A set of inactive galaxies was selected to match them in terms of host galaxy type, mass (using H-band luminosity as a proxy), inclination, presence of a bar, and distance. More details, as well as a comparison of the active and inactive galaxies, are given in Davies et al. (2015). Although small, this volume-limited sample is sufficient for detailed studies of emission line ratios, the molecular and ionized gas kinematics and distributions, as well as the stellar kinematics and populations, in the nuclear and circumnuclear regions. And the ability to compare the results to a matched sample of inactive galaxies has been essential in many of the studies so far, including the analysis presented here. These studies include the following: the physical properties of, and extinction to, the broad-line region (BLR; Schnorr-Müller et al. 2016b); the respective roles of host galaxy and environment in fuelling AGN (Davies et al. 2017); the molecular gas content and depletion time on kiloparsec scales (Rosario et al. 2018); the nuclear stellar population and kinematics (Lin et al. 2018); the black hole masses and location in the $M_{\rm BH}$–σ_* plane (Caglar et al. 2020); and the nuclear star formation histories (Burtscher et al., in preparation).

For this paper, we have limited the subsample of active galaxies to include only type 2 Seyferts (Sy types 1.8–2), which gives 11 objects. This subselection ensures that any broad line emission is weak enough that it does not limit our ability to fit the complex profiles of the narrow line profiles or to separate them from the stellar absorption features. For the analysis using the auroral and transauroral lines, we had to limit the AGN further, omitting those for which the full set of necessary [S II] and [O II] lines could not be measured reliably (ESO 021-G004, NGC 1365, and NGC 7172). This does not introduce a line ratio bias because these are simply the three objects with the faintest line fluxes. The subsample of inactive galaxies with X-shooter observations contains 18 objects. We exclude three – NGC 1315, NGC 2775, and NGC 5845 – which have no measurable line emission. Thus, there are 11 active and 15 inactive galaxies in the sample analysed in this paper.

Table 1. Summary of observations.

Object	Type[a]	v_{sys} (km s^{-1})[b]	# Obs	Dates	Seeing (arcsec)[c]
ESO 137-G034	Sy 2	2763	3	2015-05-18, 2015-05-20, 2015-06-23	1.03, 1.54, 0.80
MCG-05-23-016	Sy 1.9	2513	2	2014-01-21	1.06, 0.95
NGC 2110	Sy 2 (1h)	2329	2	2013-11-24	0.58, 0.50
NGC 2992	Sy 1.8	2328	2	2014-02-25, 2014-02-26	0.73, 0.76
NGC 3081	Sy 2 (1h)	2385	2	2014-02-19	0.58, 0.80
NGC 5506	Sy 2 (1i)	1963	1	2016-03-03	0.60
NGC 5728	Sy 2	2775	2	2015-05-12, 2015-07-15	0.81, 0.78
NGC 7582	Sy 2 (1i)	1598	2	2016-07-26, 2016-08-08	0.38, 0.72
ESO 021-G004	Sy 2	2834	1	2016-08-01	0.41
NGC 1365	Sy 1.8	1630	2	2013-12-10	1.34, 1.18
NGC 7172	Sy 2 (1i)	2568	2	2015-08-11	1.13, 1.44
ESO 093-G003	Inactive	1828	2	2014-01-21, 2014-03-20	1.44, 1.24
ESO 208-G021	Inactive	1075	2	2013-12-11, 2014-01-21	0.61, 1.05
NGC 0718	Inactive	1729	1	2015-12-04	0.60
NGC 1079	Inactive	1455	1	2013-11-22	0.80
NGC 1947	Inactive	1189	2	2013-12-22, 2014-02-07	0.67, 1.21
NGC 3175	Inactive	1099	2	2014-03-08, 2013-03-09	1.49, 0.63
NGC 3351	Inactive	781	2	2014-02-20	1.08, 1.06
NGC 3717	Inactive	1744	2	2014-03-21	1.37, 1.22
NGC 3749	Inactive	2746	2	2014-03-21, 2014-03-31	1.58, 1.46
NGC 4224	Inactive	2623	1	2015-05-12	0.79
NGC 4254	Inactive	2418	1	2016-06-01	0.42
NGC 5037	Inactive	1916	2	2015-05-12, 2016-02-03	1.18, 0.76
NGC 5921	Inactive	1484	2	2015-06-15, 2015-06-23	0.82, 0.86
NGC 7727	Inactive	1837	1	2015-08-08	0.70
IC 4653	Inactive	1535	2	2015-05-18, 2016-06-03	0.93, 0.55

[a]Classifications are taken from Davies et al. (2015) and references therein; 1i indicates that broad lines have been observed in the NIR, and 1h indicates that hidden broad lines have been detected via polarization measurements.
[b]We report heliocentric systemic velocity. The uncertainty, including systematic effects, is 13 km s^{-1}; for internal referencing, the uncertainty is typically 3 km s^{-1}. NGC 1365 and NGC 5506 are special cases, described in Section 2.6.
[c]Seeing is that reported for the beginning of the observations by the seeing monitor at the VLT. In the few cases this is not available, an alternative measurement close in time is used.

2.2 Observations and data reduction

Details of the observations, data reduction, and spectral extraction for all these objects are given in Burtscher et al. (in preparation). We have simply reused those spectra. We list in Table 1 the number of observations that was performed for each object, with their dates. Very briefly, we used the integral field unit (IFU) in X-shooter and integrated for approximately 1 h for each observation of each source. The instrument rearranges the three slitlets across the IFU to form a single slit, which is dispersed as a single 2D spectrum. The ESO pipeline version 2.6.8 (Modigliani et al. 2010) was used to process the data in its default mode. The main steps included bias subtraction, removal of the interorder background, flat-fielding, subtraction of the sky exposure, and rectification. Wavelength calibration was performed using arc lines, for which the pipeline provides wavelengths in air. For this reason, the analysis in this paper also uses wavelengths of spectral lines and features defined in air rather than vacuum (being inconsistent in this respect leads to an offset of 80 km s^{-1} when measuring systemic velocity). Because we used X-shooter in its IFU mode, the three slitlets across the IFU were then put back together to create a data cube for each arm. A 1D spectrum was extracted in a 1.8 × 1.8 arcsec^2 aperture from the UVB and VIS arms that cover 300–560 and 560–1024 nm, respectively. This aperture corresponds to 3 × 3 spatial pixels in the IFU field of view (i.e. covering its full width), and was chosen over a 1 × 1 pixel aperture to minimize the impact of imperfect positioning of the target in the IFU, variations in seeing, and to increase the signal-to-noise ratio. The location of the extraction aperture on the object was determined in the NIR arm (although those data are not used in the analysis presented here), which allows the best centring because it is least affected by extinction and, for the AGN, includes bright non-stellar continuum. For the UVB and VIS arms, the extraction aperture location was adjusted with respect to the NIR according to the mean differential atmospheric refraction during the observation. Observations of the telluric and flux calibrator stars confirmed the validity of this approach. Flux calibration and correction of telluric absorption were performed on the extracted 1D spectra. A comparison of the count rates from one particular calibration star that was observed multiple times over a period of 21 months indicates that the uncertainty in flux calibration is $\lesssim$2 per cent in the wavelength range relevant to this work. Finally, the calibrated 1D spectra from the UVB and VIS arms were merged by scaling the overlapping region to provide a consistent flux calibration over 300 nm to 1.0 μm. The spectral resolution is $R = 8600$ in the UVB arm and $R = 13\,500$ in the VIS arm. We have not corrected for this difference, partly because the unresolved line widths in both arms are rather smaller than those discussed in this paper, and also because the difference does not affect the measurement of line fluxes and ratios, nor of outflow velocities, that are pertinent to our analysis. Within the uncertainties of the small numbers analysed here, the distributions of the stellar velocity dispersion for both the active and inactive galaxies are the same, with values for individual objects in the range $\sigma_* \sim 100$–200 km s^{-1}. In all cases the measured dispersion is at least a factor of 3 greater than the instrumental broadening (more typically a factor of 6–12), and so any correction for that will have a negligible effect.

For each object, the resulting spectra from each observation were analysed separately in order to provide independent estimates of each measured property. By doing this, we are able to confirm that the uncertainties derived for these properties are consistent with the differences between the values measured from each spectrum. When more than one observation is available for an object, the resulting values reported in this paper are the mean of the values derived from the individual observations weighted by their respective uncertainties.

2.3 Stellar continuum fitting and subtraction

Many of the emission lines we measure are superimposed on stellar absorption features, which need to be removed. Since our sole aim is to remove the stellar features, we adopt a simple approach, using a theoretical library of individual stellar spectra from Coelho (2014) covering a range of temperature and surface gravity. The advantage is that the high resolution of the library enables us to retain the full resolution of the spectra.

We fit intermediate length ∼500 Å segments independently. This was done in order to avoid difficulties associated with a single very long wavelength baseline (e.g. due to irregularities in the continuum shape that arise during data processing, or assumptions such as applying only a single value of extinction to all the stellar populations), while still enabling each segment to include multiple spectral features and allowing strong emission lines to be masked or avoided. We therefore performed this step separately in advance of fitting the emission lines. Nevertheless, when fitting individual lines or doublets, we do still include a linear function that allows for adjustment of the remaining continuum baseline locally over the <100 Å regions pertinent to those lines.

We limited the range of template parameters to temperatures $4000 \leq T_{\rm eff}\,({\rm K}) \leq 7000$ and surface gravities $2.5 \leq \log g\,({\rm cm\,s^{-2}}) \leq 4$, with solar abundances. This range was selected for two reasons. It provides enough flexibility to account for the variety of continua seen in the data. But it also avoids creating a fit with overly deep Hα absorption, which is important in that spectral segment because the hot star contribution is less well constrained than in the segment with Hβ. The consistency of the fits to different spectral segments in the same object was checked by comparing the relative contributions of different stellar types for each segment. The fitting was done using the Penalised Pixel Fitting routine pPXF (Cappellari & Emsellem 2004; Cappellari 2017).

2.4 Emission and absorption line fitting

We have characterized the emission and absorption lines using one or more Gaussian functions. We emphasize that multiple Gaussian components are used only to match the observed line profiles, and we do not consider this in terms of a decomposition into different kinematic components. Indeed, in Section 3 we argue that for the observations presented here, one cannot attribute a physical meaning to the individual Gaussian components for these line profiles.

As a first step, we subtract the fitted stellar continuum over an intermediate wavelength range, as described in Section 2.3. The emission lines were then fitted using Gaussian components together with a local linear continuum. For the strong lines (e.g. Figs A4 and A5), this was done simultaneously in a single fitting process. For the weaker lines discussed in Section 4.2 (see Figs A6 and A7), there are other emission lines close around the line of interest, and so the continuum is best constrained using separate line-free regions. Therefore, for all the lines discussed in that section, the continuum was fitted separately using regions that were offset on both sides of the line of interest. The impact of the uncertainty of this linear fit was included in the uncertainty of the emission line fit. In each case the number of components used to fit the emission lines was kept to a minimum. The number was only increased if visual inspection of the residuals from the [S II] and [O III] line fits showed coherent structure above the noise level that could be substantially reduced by including another component in the fit. As such, the number of components required is simply a reflection of the complexity of the profile shape. We found that only one or two components were needed for each line in the inactive galaxies, while the active galaxies required more typically three components (and for NGC 5728 four components). In order to ensure that the local continuum level and slope was well matched, we included a linear function in the fit. This operates on the short wavelength range associated with the individual emission lines and so is independent of the stellar continuum fit described above, the purpose of which was to compensate for the complex shape associated with absorption features. We used the routine MPFITFUN (Markwardt 2009); and we propagated the uncertainties of the parameters provided by this routine to the relevant properties using Monte Carlo techniques. For doublet lines, we have applied constraints to the fit based on two main premises: (i) that the separation of the two lines is set by atomic physics, and (ii) to make sure that the profiles of the two lines in each doublet are the same. Hence when deriving a doublet line ratio, we are measuring a single ratio for the full line profile. In addition, when fitting the four doublets described in Section 4.2, we expect that the kinematic properties of the lines will be similar although not necessarily exactly like. Based on the properties of the highest signal-to-noise ratio doublet, [S II] λλ6716, 6731, we have therefore constrained the kinematic structure of the weaker doublets. Specifically for these three doublets, we have fixed the relative centring and full width at half-maximum (FWHM) of the various Gaussian components, while allowing their relative strength to vary between each doublet to provide some flexibility in terms of differences between the doublets.

Table 1 shows that three of our targets (MCG-05-23-016, NGC 2992, and NGC 1365) are type 1.8–1.9, and therefore have measurable broad line emission at Hα and in one case also at Hβ. Detailed fits to these and other H I lines have been performed by Schnorr-Müller et al. (2016b) in order to derive the extinction to the BLR and constrain the excitation. Here, we use a single Moffat function to represent the BLR, and fitted it simultaneously with the narrow lines. The example of NGC 1365, discussed later in Section 2.6, is shown in Fig. A2; the other two objects are more straightforward to fit and show no broad Hβ. The BLR properties we find are consistent with those reported by Schnorr-Müller et al. (2016b).

2.5 Uncertainties

This section outlines how we have derived uncertainties throughout the paper, and what is included in the values quoted. In general, one can consider three types of uncertainty: interpretational, systematic, and random.

Interpretational uncertainties are related to assumptions or simplifications made when analysing the data. They are discussed at the places where they arise in the paper. In terms of the systemic velocity of the galaxies, they are related to whether the spectral lines used do indeed trace the stellar population, or if there is a contribution from the ISM that might bias the measured velocity. Section 2.6 shows that this is negligible. In terms of outflow rate, interpretational uncertainties dominate. In Section 5, we highlight that the different classes of

simple outflow models differ intrinsically by a factor of 3. In addition, the adopted extinction law has an impact on dereddened line fluxes. Another common assumption is that all the gas emission within the beam or aperture comes from clouds that are identical in terms of their size, mass, internal structure, and emergent line emission. How this simplification propagates into uncertainties on the derived parameters is unknown. None of these effects are explicitly included in the quantitative uncertainties given here (nor in the literature more generally), but their existence should still be borne in mind.

Systematic uncertainties, in the context here, are associated with calibration and processing of the data. They play an important role for the systemic velocity and, as we show below, dominate the uncertainties in that case. However, for most of the analysis in this paper, we deal with velocities that are referenced internally within our own data. As such, they affect all velocity measurements in the same way and so can be ignored.

Random (or statistical) uncertainties depend on the data quality, which is largely determined by the photon and read noise. They also depend on how well the data processing procedures minimize these effects in the final data product. These uncertainties are based on formal error propagation and so it should be borne in mind that they should always be qualified as 'under the assumptions made'. This is particularly important here because the spectral resolution and signal-to-noise ratio of the emission lines we measure mean that these uncertainties are small.

When deriving the systemic velocity, we have used three methods to assess the systematic and random uncertainties. The first uses the uncertainties estimated internally by MPFITFUN for each of the three absorption lines. We have combined them to estimate a single uncertainty for each spectrum; and then further combined the values for all the spectra of each object. This yields typical uncertainties of 3 km s^{-1}. As an alternative, for each spectrum, we have calculated the standard error of the measured velocity offset of each line from their median velocity. Because only three values are available, this provides an estimate that is larger than the true uncertainty. Combining the values for all the spectra of each object yields uncertainties around 5 km s^{-1}. These are the relevant numbers to use when comparing the velocities of the emission lines to the systemic velocity. The third method we have used includes systematic effects, because it explicitly takes into account variations due to different observation times, dates, conditions, and calibrations. For the objects with two or more spectra, we have considered the difference in the estimated systemic velocity between them. The standard deviation of these differences is 13 km s^{-1}. This is the value that should be used when comparing the systemic velocity to other (external) measurements.

When estimating uncertainties on properties of the emission lines, we have also made use of the uncertainties derived internally by MPFITFUN. These correspond to parameters of the component Gaussians and the linear continuum. Since, as described in Sections 2.3 and 2.4, the continuum is fit in two steps, it is important to note that the residual structure from the initial fit is taken into account when evaluating the noise in the spectrum, and that the residual offset and slope are removed by the second local fit. The parameter uncertainties are used to create 1000 realizations of the line profile. In this Monte Carlo approach we implicitly make the conservative assumption that these uncertainties are uncorrelated. The suite of line profiles then allows an estimate of the uncertainty on the higher level properties used in our analysis, which focus on line fluxes, ratios, and velocities. We have performed a cross-check on this process using a simple and robust independent estimate of the zero moment and its error. We define a spectral region where the fitted line flux is above 5 per cent of its peak, and measure the line flux within this region. We also measured the noise of the residual, which, scaled by the square root of the number of pixels, yields the uncertainty of the line flux. While this method is simple and robust, it cannot take into consideration the constraints included in the fitting procedure, for example that the profiles of the two lines in the doublet are tied so that they are the same. Thus, while one can expect the error estimates to be generally comparable, one should also expect that there are some differences. This is what we find for all the lines on which we have performed the comparison, namely the [S II], [O II], and [O III] doublets, and the Hβ line. We conclude that while the uncertainties due to random noise in the data are very small, this is a reflection of the data quality in the spectra.

2.6 Systemic velocities

A measure of each object's systemic (heliocentric) velocity, $v_{\rm sys}$, which is independent of the emission lines, is an important aspect of the analysis presented here. For all except two of the objects, we have used the Ca II triplet lines since these are strong in a wide variety of stellar types, relatively narrow, and generally free from strong line emission, making them an ideal tracer of internal stellar kinematics (Dressler 1984). And in contrast to the Ca II H&K lines, they are not contaminated by interstellar absorption. This is illustrated for measurements of star cluster F in M82 by Gallagher & Smith (1999), who found that the Ca II K line had a velocity that differed by 150 km s^{-1} from the triplet lines. The former matched Na I D while the latter velocities were similar to Mg I b. We fitted a Gaussian profile separately to each of the Ca II triplet lines at 8498, 8542, and 8662 Å, including a local estimate of the continuum as part of the fit as described in Section 2.4. These can be seen in Fig. A1.

In the case of NGC 1365 and NGC 5506, the Ca II features were filled with strong Paschen H I emission. Instead, for these two objects we have explored other features to estimate $v_{\rm sys}$. These are specifically the Mg I b triplet around 5175 Å, the Na I D doublet around 5890 Å, and the K I doublet around 7680 Å. The Mg I lines are strong in the spectra of K–M-type stars, and generally absent from interstellar absorption spectra. The Na I, and especially K I, lines are present in the spectra of cooler stars but need to be treated cautiously because they can also arise from, and in some cases are dominated by, interstellar absorption (Hobbs 1974; Schwartz & Martin 2004; Rajpurohit et al. 2014). This means that any estimate of systemic velocity using these lines may be biased by a contribution from a neutral outflow (Rupke, Veilleux & Sanders 2005a,b).

For NGC 1365, inspection of these regions (see Fig. A2) shows that the latter are dominated by the ISM while the Mg I lines are too weak to fit reliably. We have instead used the systemic velocity adopted by Venturi et al. (2018), because this yields a symmetric stellar velocity field over the central arcminute of the galaxy (Venturi, private communication), which is a robust way to derive $v_{\rm sys}$. As a visual confirmation of this value, we note that the Mg I lines are consistent with the wavelengths it implies. In contrast the Na I and K I lines are seen at velocities corresponding to -110 and $+50$ km s^{-1}. That absorption can be both redshifted and outflowing is possible if it is tracing the receding bicone against an extended stellar continuum. It is notable from Fig. A2 that the velocity of the fit to the broad emission line matches that of the blueshifted absorption component, while the narrow emission lines are more associated with the redshifted absorption component. Such an association between ionized and neutral components in an outflow has been analysed in detail for a post-starburst E+A galaxy using spatially resolved data by Baron et al. (2020). In closing, we note that many references in the NASA/IPAC Extragalactic Database (NED) give redshifts closer to 1660 km s^{-1}, which matches the velocity we measure for the narrow

emission lines. As our analysis in Section 3 shows, this offset arises because the peak of the emission lines does not necessarily trace the systemic velocity.

For NGC 5506 the optical spectrum (see Fig. A3) shows an almost featureless continuum. This suggests that one should be cautious of the systemic velocity of 1750 km s^{-1} quoted by Van den Bosch et al. (2015) because it was based on fitting the stellar continuum. Instead, we have searched for a well-defined narrow stellar feature that can be robustly measured. The only clear features are the Na I and K I absorption, which appear to be composed of a series of narrow lines. Based on our spectra of the other galaxies, estimating the systemic velocity from the Na I line in our sample yields a modest bias of $<$10 km s^{-1} although the scatter for individual objects is higher. In the absence of other tracers, we estimate $v_{\rm sys}$ = 1962 km s^{-1} using that doublet, and assess whether it is consistent with expectations. Crucially, the emission line profiles – especially [O III] – show a distinctive dip at this velocity. In Section 3, we show that many of the AGN line profiles have a similar form, with the dip at systemic velocity. As we argue there, in models this represents the transition between the approaching and receding sides of bicone outflows. As such, we take this as confirmation that the systemic velocity is close to our estimate. In closing, it is worth noting that there are a large number of redshift measurements in NED, typically giving 1800–1850 km s^{-1} based on optical emission lines. However, the emission line peaks are blueshifted with respect to our estimate of $v_{\rm sys}$; and fitting our data with a single Gaussian would yield a velocity for the line peak of 1810 km s^{-1}, consistent with the published values such as 1829 km s^{-1} (de Vaucouleurs et al. 1991), 1853 km s^{-1} (Keel 1996), and 1828 km s^{-1} (Koss et al. 2017).

The systemic velocities we measure are given as heliocentric velocities in Table 1. Most of these are consistent with the values reported in the literature by NED. However, in addition to NGC 1365 and NGC 5506 where we have referred to the literature to estimate $v_{\rm sys}$, there were three galaxies where the difference exceeded 100 km s^{-1}. We have checked these in order to confirm our measurements as follows.

2.6.1 *ESO 021-G004*

The only redshift in NED is 2960 km s^{-1} from an H I measurement. The H I source was matched to ESO 021-G004 by Doyle et al. (2005), but its coordinates put it about 65 arcsec from the galaxy centre, beyond the optical size of the galaxy. Therefore, while the H I source may indeed be associated with this galaxy, we recommend caution with the cross-identification.

2.6.2 *NGC 5037*

The value adopted by NED is based on an H I measurement from Pisano et al. (2011). This is likely a misidentification, since the coordinates of the galaxy do not match those listed for it in their table 2. Instead, the velocity of 1904 km s^{-1} given in de Vaucouleurs et al. (1991) and the 1890 km s^{-1} reported by Mendel et al. (2008) are consistent with the velocity we find.

2.6.3 *IC 4653*

A redshift of 1890 km s^{-1} is given in de Vaucouleurs et al. (1991), but a more recent measurement of 1551 km s^{-1} based on the Mg II feature was reported by Wegner et al. (2003). Although both of these have sizeable uncertainties (87 and 55 km s^{-1}, respectively), it is difficult to account for such a large difference between them. We note that for this inactive galaxy, our data are characterized by a narrow line profile for both stellar absorption and line emission, which are centred at very similar velocities and show no indication for an outflow. The systemic velocity implied by these features is consistent with that reported by Wegner et al. (2003).

3 INTERSTELLAR MEDIUM VERSUS OUTFLOW

In this section, we discuss whether the emission line profiles shown in Fig. 1 are dominated by the interstellar medium (ISM) or the outflow; and whether, for the AGN, there is in fact any measurable ISM component. When referring to the ISM, we mean the ambient gas in the circumnuclear disc of the host galaxy. When referring to the outflow, we mean any gas that is not just photoionized by the AGN, but also kinematically disturbed by it. Spatially resolved studies (Fischer et al. 2017, 2018) have shown that there may be threshold radii, with gas closest to the AGN being driven out, beyond this a region where gas is still kinematically disturbed by the AGN, and finally a region where gas is photoionized by the AGN but remains undisturbed kinematically. Fischer et al. (2018) reported that for their sample of AGN, kinematically disturbed gas is seen out to $\sim$1.1 kpc. Our line profiles are integrated over a 1.8-arcsec box that corresponds to a much smaller radius of $\sim$150 pc. Even though, based on $L_{\rm [O\,III]}$, the AGN in our sample are an order of magnitude less luminous, we would still expect that at these radii the kinematics should be dominated by the AGN rather than the host galaxy. In the following, we examine whether the excitation and kinematical properties of the AGN emission lines, in comparison to the matched inactive galaxies, support this assumption.

3.1 Excitation

The left-hand panel of Fig. 2 shows the standard [N II]/Hα versus [O III]/Hβ ratios for our sample. For this plot, we used the flux integrated over the full line profile, and so it simply shows that the whole of the line emission is dominated by AGN photoionization rather than other processes. Although some AGN lie close to the border with the region occupied by low-ionization nuclear emission-line region (LINER) galaxies, it is known that there is considerable overlap between Seyferts and LINERs at that boundary (Kewley et al. 2006). The line equivalent width should be considered a third dimension of the standard line ratio plot because it shows that, at high [N II]/Hα ratios, AGN photoionization is generally associated with much brighter line emission than would be expected from photoionization by post-asymptotic giant branch (AGB) stars (Stasińska et al. 2008). Cid Fernandes et al. (2010, 2011) proposed its use in an alternative and complementary 'WHAN' diagnostic plot of the Hα equivalent width versus the [N II]/Hα ratio. This is shown for our sample in the right-hand panel of Fig. 2, where the AGN and inactive galaxies form distinct sequences. The location of the AGN in these two plots confirms that their emission lines are indeed AGN dominated. The only exception is ESO 021-G004, which has a remarkably low Hα equivalent width. This is surprising because the sample selection ensures that all the AGN are of similar moderate luminosity, and Table 6 shows that ESO 021-G004 is unremarkable in this respect. Instead, our estimate of the extinction to the narrow lines based on the Hα/Hβ ratio given in Table 4 indicates that this object (together with NGC 7172) has $A_{\rm V} > 3$ mag and hence its intrinsic line luminosity is a factor of 15 higher than that observed.

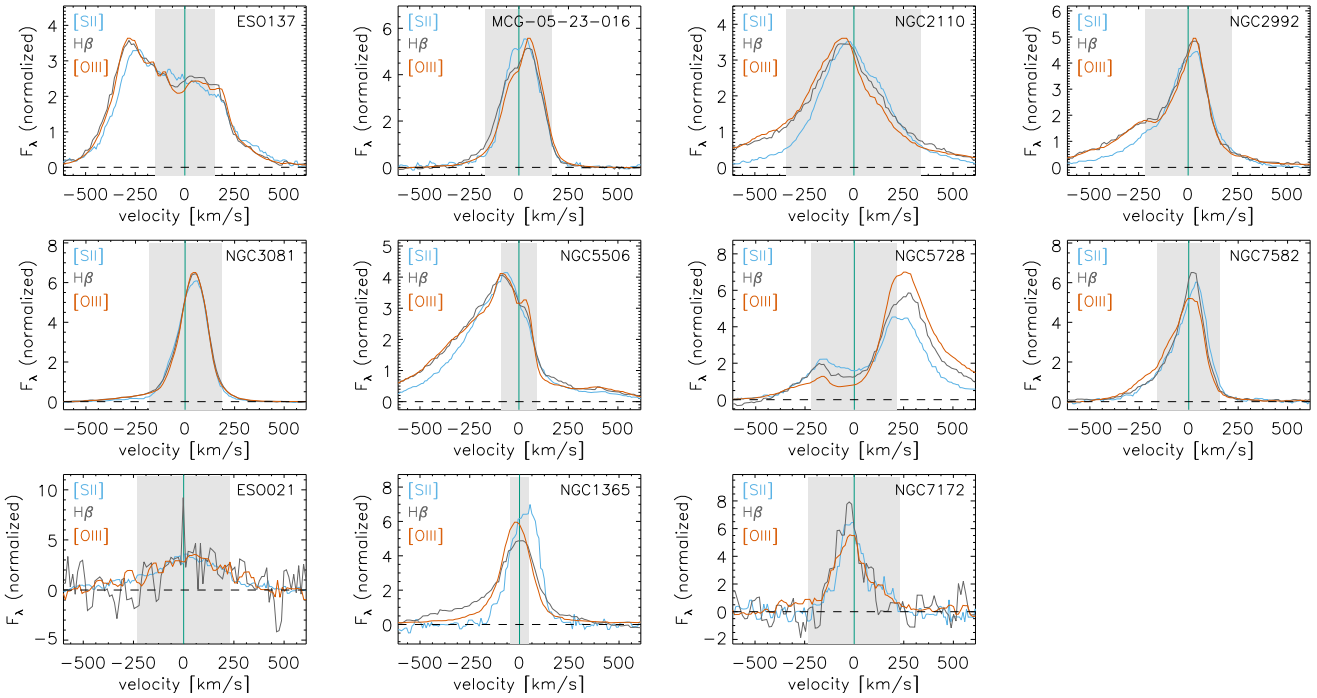

Figure 1. Comparison of the central part of the line profiles of the AGN as a function of velocity, normalized so that they have the same flux within ± 250 km s^{-1}. The Hβ, [O III], and [S II] profiles are shown in grey, red, and blue, respectively. For visualization purposes, the [S II] profile is a combination of the short side of the 6716 Å line and the long side of the 6731 Å line, scaled to match where they overlap. These plots are of the data only, and not the fits. For reference, the FWHM of the stellar absorption profile is indicated by the shaded grey region. It is clear from this plot that the profiles show a variety of shapes that are generally inconsistent with the 'systemic+outflow' decomposition often adopted. We argue that the whole profile is dominated by, and hence traces, outflow. For reference, similar plots of the line profiles for the inactive galaxies are shown in Fig. A8 of Appendix A.

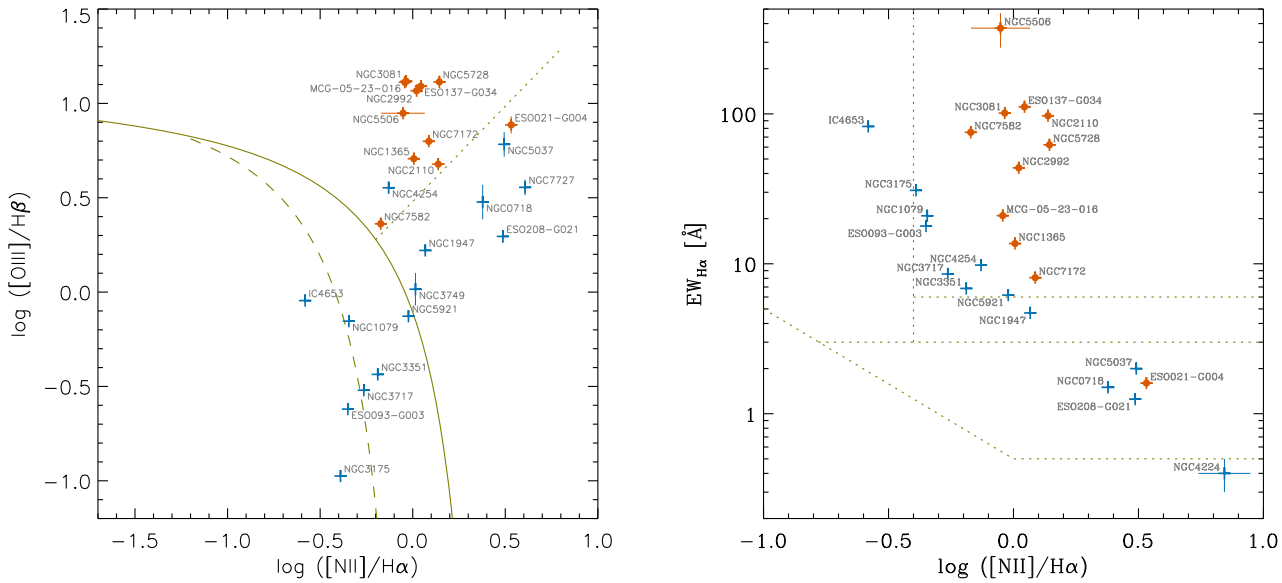

Figure 2. Comparison of measured emission line quantities for AGN (red with filled circles) and inactive galaxies (blue). Left: standard [N II]/Hα versus [O III]/Hβ diagnostic ratios, with the Kewley et al. (2001) extreme starburst line (solid) and Kauffmann et al. (2003) classification line (dashed), as well as the Cid Fernandes et al. (2010) Seyfert/LINER coarse separation (dotted). Among the inactive galaxies, NGC 4224 is omitted because Hβ was not detected. Right: the WHAN plot of the equivalent width of Hα versus the [N II]/Hα ratio. The dotted lines are shown for reference to figs 1 and 6 of Cid Fernandes et al. (2011). The key point here is that the AGN and inactive galaxies form distinct sequences. These panels show that the emission lines in the AGN sample are dominated by the AGN photoionization.

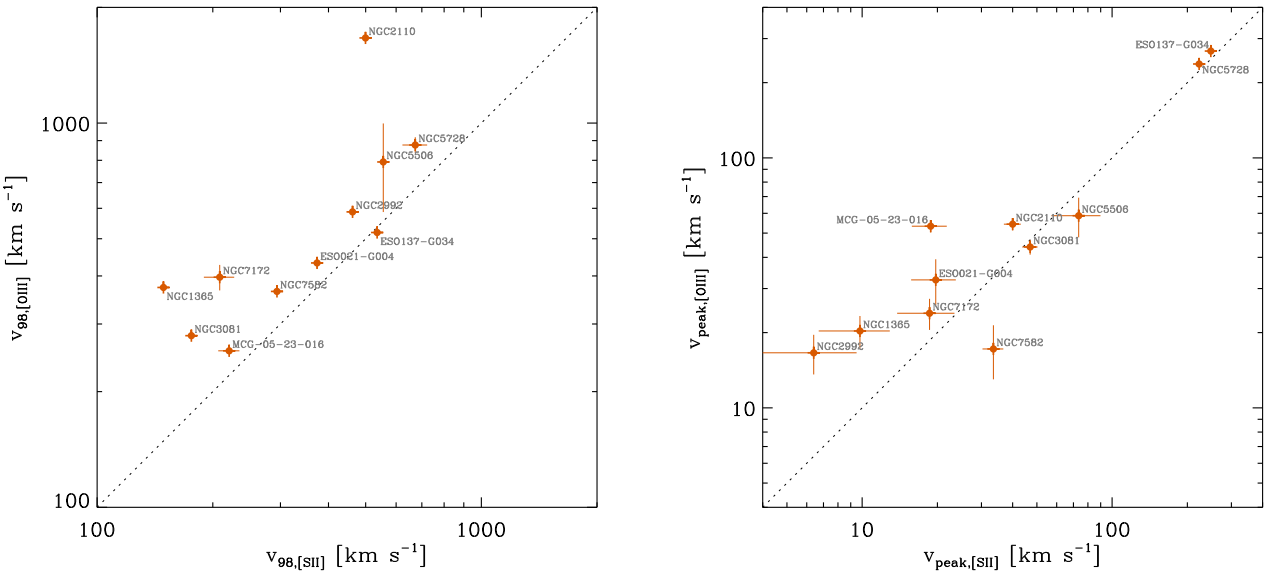

Figure 3. Comparison of the [S II] and [O III] emission lines for the AGN, in terms of peak offset v_{peak} from systemic (left) and outflow velocity v_{98} (right). The dotted lines indicating a 1:1 correspondence show that in each case the two lines are very similar. These show that there is little difference between the kinematics traced by these two emission lines. The left-hand panel reflects the well-known result that [O III] has broader wings than [S II] (Veilleux 1991); in this case the velocity difference is about ∼25 per cent. Only NGC 2110 is an outlier, and inspection of Fig. 1 shows that its [O III] line does have very broad wings. In the right-hand panel, the peak velocity offsets are well correlated to 10–20 km s^{-1} which is the expected level of systematics.

The inactive galaxies occupy a rather different locus on these plots, following a relatively narrow track that extends from pure star-forming galaxies to LINERs photoionized by post-AGB stars. This sequence clarifies that NGC 4254, while it is formally among the Seyferts in the left-hand panel of Fig. 2 (bearing in mind that there is overlap with LINERs across that boundary), does indeed fit better among the inactive galaxies. These objects were selected to be matched to the AGN host galaxies (Davies et al. 2015; Rosario et al. 2018) and so are similar on large scales. An analysis of the stellar population in the central ∼300 pc shows that they are also similar on small scales (Burtscher et al., in preparation). These studies imply that if the AGN were to become inactive, we would expect them to look like the inactive sample, with similar photoionization properties and line strengths. This difference is apparent also in the kinematics, as discussed next.

3.2 Velocities

To quantify the line kinematics, we define two properties that are measured relative to the systemic velocity defined by stellar absorption features.

v_{peak} is the velocity offset from systemic of the peak of the emission line. It has the same role as v_{int} (line centroid) used by Bae & Woo (2016) in their analysis of line profiles in biconical outflows. We use it to determine whether or not the core of the line is tracing the ambient ISM or the outflow.

v_{98} is the velocity above (or below) which one finds 98 per cent of the line flux. We compare the absolute values of these and use whichever is the larger (we do not distinguish between the red and blue wings, and so v_{98} as used here does not have a sign). This is motivated by the need to reliably estimate the maximum outflow velocity. It is similar in concept to other commonly used metrics (Rupke & Veilleux 2011; Liu et al. 2013; Veilleux et al. 2013; Perrotta et al. 2019), and is an appropriate measure for the complex line profiles encountered here.

We have derived these for [S II], rather than the standard outflow tracer [O III], because it is well detected in both active and inactive galaxies, allowing a comparison of these subsamples. In order to assess the level of bias in using [S II], Fig. 3 compares v_{peak} and v_{98} for the two lines in the AGN. With the exception of NGC 2110, there is good agreement between them, the most notable difference being that v_{98} for the [O III] line is about 25 per cent larger (see also a comparison of the line profiles in Fig. 1).

The distributions of v_{98} and v_{peak} are shown in Fig. 4. The active and inactive galaxies have rather similar distributions of v_{98}. The reason is that for the inactive galaxies, it traces the edge of an outflow wing in the line profile that is distinct from the dominant systemic component. In contrast, for the active galaxies, the outflow is the dominant part of the line profile, and so v_{98} traces the edge of the bulk of the line emission. This is clarified by the distribution of v_{peak}. For inactive galaxies, the median absolute offset of the line peak from systemic is only 11 km s^{-1}. Such small values are consistent with irregularities in a distribution that basically traces host galaxy rotation. It strongly suggests that the line peak for inactive galaxies is tracing the ambient ISM, as expected. In contrast, the offsets for almost all the AGN are larger than the median of the inactive galaxies; and for more than half of the AGN they are greater than the maximum 28 km s^{-1} for the inactive galaxies. The median of 34 km s^{-1} for the AGN is a significant offset for the line peak and, if associated with host galaxy rotation, would imply a highly asymmetric (one-sided) line distribution. Instead, we conclude that in the central few hundred parsecs of AGN, even the peak of the emission lines is tracing outflow.

3.3 Outflowing versus ambient gas

The line profiles of some AGN, typified by NGC 5728 and ESO 137-G034, are characterized by a wide double-peaked profile either side

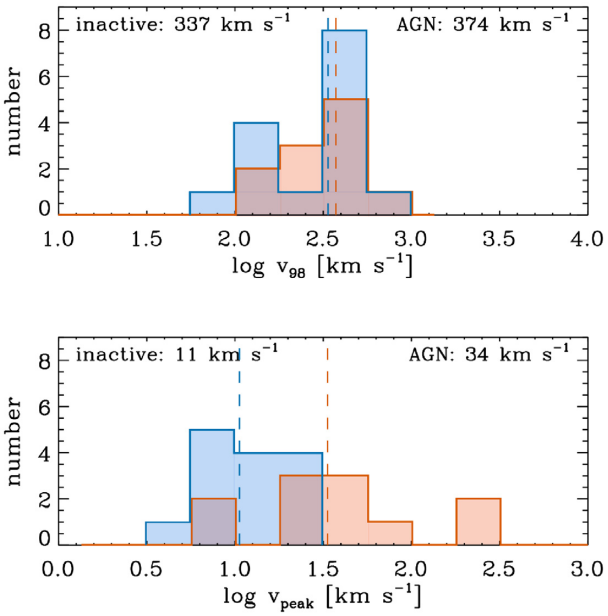

Figure 4. Comparison of kinematic emission line properties for AGN (red) and inactive galaxies (blue), with median values indicated by the vertical dashed lines. Upper: maximum velocity $v_{98,[S\,II]}$ of the [S II] line from systemic. Lower: velocity offset $v_{peak,[S\,II]}$ of the peak of the [S II] emission line from systemic (as measured by stellar absorption features). Both quantities are given as absolute values. These show that v_{98} is similar for the active and inactive galaxies, while v_{peak} distinguishes between them rather well. This is because the high value of v_{98} for the inactive galaxies is due to an outflow wing on the line profile that is distinct from the systemic component; while for the AGN the outflow is the dominant part and so affects v_{peak} as well.

of systemic, which can be understood in terms of the approaching and receding sides of an outflow. In these objects any systemic contribution to the line is negligible. A library of line profiles from biconical outflows has been modelled by Bae & Woo (2016), covering a variety of orientations, opening angles, and differential extinction. Although at lower resolution than our spectra, they show clearly that, in addition to complex profiles such as those discussed above, one can expect some outflows to have rather narrow unremarkable profiles because of their more edge-on orientation. This is particularly important for type 2 Seyferts, which are by definition closer to edge-on. We have reproduced some examples at a higher resolution in Fig. 5. These cover inclinations from 40° to 80° and have the emission from behind a host galaxy disc blocked by varying amounts. They qualitatively match the profiles we observe, for example the red profile in the left-hand panel ($i_{out} = 40°$, with half of the emission behind the disc blocked) is similar to ESO 137-G034, while the green profile in the right-hand panel ($i_{out} = 80°$, with all of the emission behind the disc blocked) is more like NGC 7582. Generally, these model profiles include not only double-peaked profiles, but also narrower profiles, both with and without prominent wings. This helps understand some of the less remarkable profiles such as those for MCG-05-23-016 or NGC 3081, both of which clearly show some characteristics of outflow. In particular, MCG-05-23-016 shows a distinct break at systemic typical of a double peak from a more inclined bicone, while for NGC 3081 the profile is smoother but its peak is far offset from systemic suggesting that the approaching side may be obscured behind the galaxy disc.

As a final check about whether there is a measurable systemic component, we have examined the [S II] doublet ratio, and also the [O III]/Hβ ratio (which directly affects the derived density for the *logU* method) as a function of velocity. There are clearly trends with velocity (similar to those reported by Veilleux 1991), especially between the redshifted and blueshifted emission, reflecting differences in the approaching and receding sides of the outflow. However, even at the spectral resolution and signal-to-noise ratio of these data, there is no evidence for changes in either ratio associated with the systemic velocity. Together with the assessment of the profile shape above, this suggests that integrating over the full line profiles will not lead to any bias in the resulting density due to a (subdominant) systemic component in the line profile.

Our conclusion in this section is that while a 'systemic+outflow' decomposition can be appropriate in many cases, it cannot be meaningfully applied to the nuclear observations of active galaxies presented here. Instead, the multiple Gaussian components can only be considered together, in terms of a convenient way to characterize a complex line profile. Indeed, the observed emission lines are fully dominated by an AGN photoionized outflow. The reasons include: (i) that our spectra are extracted from small apertures that trace gas within ∼150 pc from moderately luminous AGN; (ii) our ability to make an independent measure of the systemic velocities from the stellar continuum; (iii) the complexity of the line profiles in Fig. 1 that either have a dip at the systemic velocity or continue smoothly across it; and (iv) that we know it is easy to find reasonable parameter sets for biconical outflow models that reproduce both the dramatic and the more unremarkable profiles. Our interpretation is that in every case, the whole profile is probing outflowing gas. As such, for the analysis of the outflow density in Section 4 we use the full integrated line flux.

4 DENSITY AND MASS MEASUREMENTS

In this section, we explore three independent ways to measure the density of the ionized gas. These include the most commonly used method based on the [S II] doublet ratio, an alternative proposed by Holt et al. (2011) that uses a combination of [S II] and [O II] line ratios, and a method recently introduced by Baron & Netzer (2019) that is based on the ionization parameter. We indicate their main limitations and merits, and calculate the density ranges for our sample using each method. We compare these ranges, and use photoionization models to understand the differences between them and the impact on the implied ionized gas mass.

4.1 [S II] doublet ratio method

The most commonly used electron density tracer (here referred to as the *doublet* method) uses the [S II] λλ6716, 6731 Å doublet, because it only requires a measurement of the ratio of two strong emission lines in a convenient and clean part of the optical spectrum, and the physics of the excitation and deexcitation means that density – covering a range commonly found in H II regions – dominates the emitted line ratio (Osterbrock 1989). An additional advantage is that, because the lines are necessarily close in wavelength, the derived density is unaffected by extinction.

There are, however, situations where this ratio can give misleading results. Because the two lines are separated by only 14.4 Å, corresponding to 650 km s^{-1}, deblending the doublet can become unreliable at moderate spectral resolution. This is particularly important for complex line profiles. As an example, in a detailed study of the ionized and molecular gas in the circumnuclear region of NGC 5728,

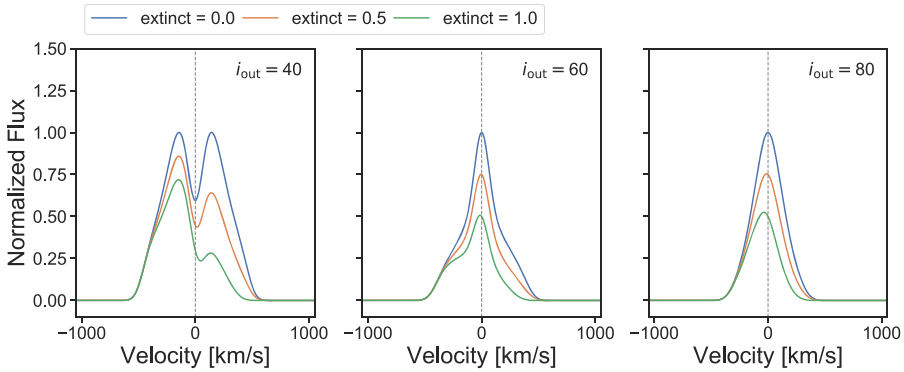

Figure 5. Examples of the variety of line profiles that can be produced by a biconical outflow, depending on orientation (panels are for $i_{out} = 40°, 60°, 80°$ to the line of sight) and dust obscuration (colours denote a fraction *extinct* = 0, 0.5, 1 of the emission from behind the host galaxy disc is blocked). These particular examples are for a bicone with inner and outer half-opening angles of 20° and 40°, with a velocity profile that accelerates to 500 km s^{-1} at a turnover radius and then decelerates. A host galaxy disc oriented at 60° provides obscuration. This can affect not just the rear cone, but also produce more complex effects in the line profile if part of each cone is obscured. A full library at lower velocity resolution is presented by Bae & Woo (2016). The examples here include double-peaked profiles, as well as rather narrower profiles, both with and without prominent wings. They demonstrate that even the narrower profiles among our AGN are consistent with an outflow origin.

Shimizu et al. (2019) compared several methods of measuring the electron density using both high and moderate resolution data. They showed that for data with $R < 4000$, blending of the [S II] line profiles in this object leads to an increasing discrepancy in the derived density at smaller radii – with an order of magnitude underestimation at radial scales below 500 pc. For our sample, Fig. A4 shows that the high spectral resolution and signal-to-noise ratio of our data mean that the line profiles of both active and inactive galaxies can be robustly determined.

It is well known that [S II] cannot probe high densities because collisional deexcitation dominates above 10^4 cm^{-3} where the ratio saturates at ∼0.45, its asymptotic value. We note that this effect should not bias our measurements because none of the electron densities derived from the [S II] doublet in our sample exceed 1000 cm^{-3}.

A less well-known bias can arise from the impact of the stellar continuum when the equivalent width of the [S II] lines is low. This is illustrated in Fig. 6 for NGC 7727. The apparent line ratio of 0.98 (left-hand panel) is rather less than the actual line ratio of 1.21 (centre panel) due to the stellar absorption feature under the 6716 Å line. It seems likely that this is dominated by Fe I (Barbuy, Trevisan & de Almeida 2018). Since the feature is weak, it only affects lines with equivalent width $\lesssim$10 Å. But the impact on the resulting derived densities can be significant. For the inactive galaxies in our sample, for which the median equivalent width is 1.5 Å, the right-hand panel of Fig. 6 shows that failing to correct for this effect leads to a factor of 2.5 overestimation of the typical density. In contrast, for the stronger lines in the AGN the bias is negligible.

An additional caveat is that this method yields the electron density in the region where the line is emitted. In AGN, the emission from low ionization transitions such as [S II], [N II], and [O I] is enhanced (compared to H II regions around stars) by an extended partially ionized zone (Osterbrock 1989). In such regions of a cloud, where the gas is mostly neutral, the electron density will not necessarily be comparable to the hydrogen gas density. In some circumstances this can become a critical issue and we return to it in Section 4.4.

We have measured the [S II] doublet lines in the inactive galaxies as described in Section 2.4, constraining the profiles of the two lines in the doublet to be the same. The profile fits for the active and inactive galaxies are shown in Fig. A4 and the measured properties of the [S II] doublet lines are summarized in Table 2. The median density for the inactive galaxies is 190 cm^{-3}, while that for the active galaxies is 350 cm^{-3}. A quantitatively similar result using the [S II] doublet was reported by Mingozzi et al. (2019) who, for spatially resolved data of nine nearby AGN, reported that the mean density of 250 cm^{-3} in the outflows was higher than the mean of 130 cm^{-3} for the circumnuclear discs.

In terms of density and outflow velocity, NGC 4224 has characteristics more like an AGN outflow than the inactive galaxy that it is. It is excluded from the left-hand panel of Fig. 2 because Hβ was not detected. However, its ratio log [N II]/Hα ∼ 0.85 would put it well into the LINER region. We have found no evidence that this object might be an AGN, and indeed it has a very low Hα equivalent width of <0.5 Å. Although it is a spiral galaxy classified as Sa (Davies et al. 2015), it is one of the few inactive galaxies in our sample for which the central optical spectrum in the IFU field of view shows no indication of any stellar population younger than ∼3 Gyr (Burtscher et al., in preparation). And despite being a member of the Virgo Cluster (Binggeli, Sandage & Tammann 1985), the outer parts of the galaxy show no signs of being disturbed (Buta et al. 2015). The line characteristics indicate that there is an outflow, and we speculate that it could be driven either by post-AGB stars or a fossil AGN, perhaps as a result of rapid variability (Matt, Guainazzi & Maiolino 2003; Förster Schreiber et al. 2014; Fluetsch et al. 2019).

4.2 Auroral and transauroral line method

To avoid the limitations of the [S II] doublet ratio, Holt et al. (2011) proposed an alternative method that has now been applied to a variety of different types of objects, and been shown to be sensitive to higher densities (Holt et al. 2011; Rose et al. 2018; Santoro et al. 2018; Shimizu et al. 2019). We will refer to this as the *TA* method because it uses the transauroral lines [S II] λλ4069, 4076 and the auroral lines [O II] λλ7320, 7331 (each of the lines within this 11 Å separation doublet is itself a doublet, but their separations of ∼1 Å are sufficiently small that at the spectral resolution here they can be considered single lines), which have higher critical densities. These are used together with the stronger lines to give the ratios [S II] λλ(4069+4076)/[S II] λλ(6716+6731) and [O II] λλ(3726+3729)/[O II] λλ(7320+7331).

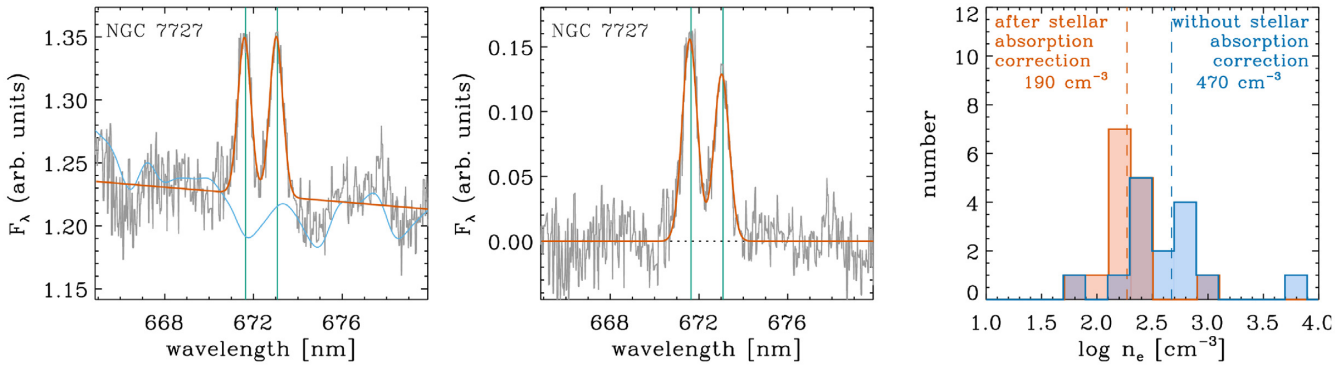

Figure 6. Bias in density measurement for a weak [S II] doublet. Left: the observed spectrum (grey line) for NGC 7727 overplotted with the stellar continuum (blue line) and a fit to the emission line doublet approximating the stellar continuum with only a linear function (red line). The vertical green lines indicate the line centres for the doublet. Centre: as for the left panel but after subtracting the fitted stellar continuum. Right: the derived densities for all the inactive galaxies without (blue) and after (red) correction for the stellar continuum.

Table 2. Measurements of [S II] doublet, and derived densities, for active and inactive galaxies.

Object	$v_{98,[S\,II]}$ (km s^{-1})	$v_{peak,[S\,II]}$ (km s^{-1})	EW$_{[S\,II]}$[a] (Å)	[S II] doublet ratio	log n_e (cm^{-3})
ESO 137-G034	536 ± 5	248 ± 3	39.6 ± 0.3	0.96 ± 0.01	2.76 ± 0.01
MCG-05-23-016	221 ± 14	19 ± 3	4.9 ± 0.1	0.98 ± 0.01	2.74 ± 0.01
NGC 2110	499 ± 7	40 ± 3	51.4 ± 0.7	1.09 ± 0.02	2.54 ± 0.03
NGC 2992	461 ± 14	6 ± 3	16.3 ± 0.3	1.02 ± 0.02	2.66 ± 0.02
NGC 3081	176 ± 3	47 ± 3	23.4 ± 0.6	0.99 ± 0.03	2.72 ± 0.05
NGC 5506	555 ± 11	74 ± 16	111.8 ± 3.3	1.17 ± 0.04	2.37 ± 0.08
NGC 5728	673 ± 50	223 ± 4	18.9 ± 0.5	1.11 ± 0.07	2.49 ± 0.14
NGC 7582	294 ± 7	34 ± 3	9.5 ± 0.2	0.96 ± 0.03	2.77 ± 0.04
ESO 021-G004	374 ± 6	20 ± 4	2.0 ± 0.2	1.22 ± 0.03	2.26 ± 0.07
NGC 1365	149 ± 3	10 ± 3	1.6 ± 0.1	1.24 ± 0.02	2.22 ± 0.04
NGC 7172	209 ± 19	19 ± 5	2.0 ± 0.3	1.25 ± 0.19	2.20 ± 0.73
ESO 093-G003	140 ± 5	15 ± 3	3.4 ± 0.1	1.18 ± 0.04	2.36 ± 0.08
ESO 208-G021	548 ± 18	11 ± 4	1.7 ± 0.1	1.17 ± 0.06	2.38 ± 0.14
NGC 0718	471 ± 128	10 ± 3	0.8 ± 0.1	1.16 ± 0.06	2.41 ± 0.13
NGC 1079	152 ± 3	6 ± 3	3.5 ± 0.1	1.27 ± 0.02	2.13 ± 0.04
NGC 1947	537 ± 44	10 ± 3	4.1 ± 0.3	1.25 ± 0.07	2.20 ± 0.19
NGC 3175	106 ± 4	9 ± 3	4.1 ± 0.1	1.23 ± 0.05	2.23 ± 0.12
NGC 3351	248 ± 23	0 ± 3	1.2 ± 0.1	1.22 ± 0.04	2.27 ± 0.09
NGC 3717	474 ± 28	28 ± 3	1.9 ± 0.1	1.23 ± 0.03	2.25 ± 0.06
NGC 3749	407 ± 31	11 ± 4	0.9 ± 0.1	1.26 ± 0.08	2.17 ± 0.25
NGC 4224	595 ± 39	16 ± 9	0.9 ± 0.1	0.83 ± 0.04	2.98 ± 0.07
NGC 4254	144 ± 12	28 ± 4	1.0 ± 0.2	1.12 ± 0.17	2.49 ± 0.35
NGC 5037	337 ± 6	28 ± 4	1.8 ± 0.1	1.30 ± 0.03	2.02 ± 0.11
NGC 5921	392 ± 13	7 ± 3	1.9 ± 0.1	1.16 ± 0.03	2.39 ± 0.06
NGC 7727	332 ± 7	25 ± 4	1.1 ± 0.3	1.21 ± 0.04	2.29 ± 0.10
IC 4653	69 ± 3	3 ± 3	12.9 ± 0.1	1.37 ± 0.01	1.72 ± 0.06

Notes. Quoted uncertainties are from formal error propagation based on the random noise in the spectrum.
[a]EW$_{[S\,II]}$ is for the 6716 Å line in the doublet.

The way these lines are used to estimate density differs fundamentally from the *doublet* method. Rather than providing a direct measure of n_e in the gas where the line emission originates, the ratios of summed doublet fluxes are compared to those produced in photoionization models. By design, such models take account internally of how n_e (on which the emitted lines depend) varies through the cloud, and hence how the resulting cumulative line ratios are related to n_H. In this way the method traces n_H rather than n_e in a cloud; but typically one equates n_H and n_e as if the gas were fully ionized. The [O II] lines arise predominantly in the fully ionized gas, but they are far apart in wavelength and so the impact of extinction needs to be addressed. This is done using the [S II] lines, which originate from different regions of the cloud and span a shorter wavelength range, so that their ratio has a different dependency on density and extinction. The pair of ratios then provides a reference basis for photoionization model grids in which density and extinction are approximately orthogonal.

The primary advantages of the method are that it is sensitive to higher densities, which is now known to be important when measuring outflow rates; and it uses the summed flux in each doublet and thus is less sensitive to the details of the line profile. However, it too has some limitations. Most critically from the observational perspective, the auroral and transauroral lines are very weak. Figs A6 and A7 show that their flux is typically only about 10 per cent of

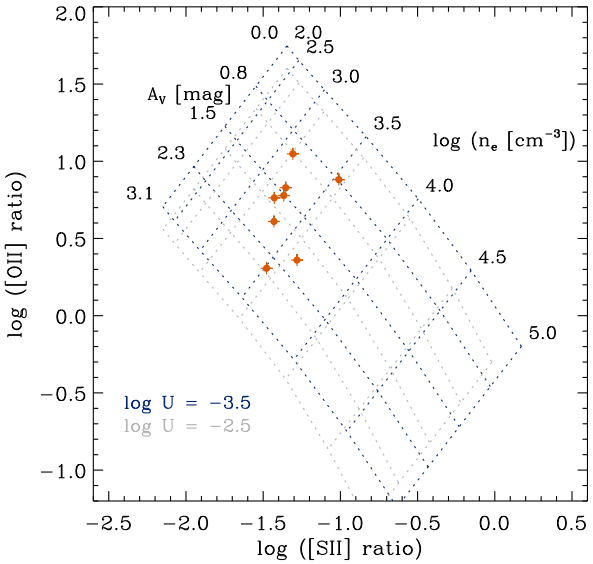

Figure 7. Location of the measured [O II] and [S II] ratios for the AGN in our sample, in comparison to photoionization models that trace a grid of extinction A_V versus electron density n_e. Models are shown for solar metallicity and a standard AGN spectral energy distribution (SED); but for two different ionization parameters covering the range found for the AGN here.

the strong [S II] and [O II] lines, and so signal-to-noise ratio can be a major restriction. For the same reason, the continuum level fitted around the lines can have a significant impact on the measured line flux and so subtracting the stellar continuum is mandatory.

The conversion of the measured ratios to a density is also not as straightforward as for the [S II] doublet ratio because it depends on photoionization models. Holt et al. (2011) assessed the impact of changes in the spectral index and ionization parameter, and argued that they are relatively unimportant. Our own calculations (described below) indicate that these should not be ignored. Fig. 7 shows that the ionization parameter can change the derived density by a factor of 2–3; and changing the metallicity has a comparable impact. In addition, the wide wavelength range required to cover all the lines means that the effects of extinction must be included when fitting the models to the data. And the choice of extinction model will also have an impact on density derived from the line ratios.

For the AGN in which all the necessary lines can be measured, we have fitted the [S II] and [O II] doublets in a similar way as before, including the various constraints described in Section 2.4. The resulting profile fits for each doublet are shown in Figs A6 and A7. As before we propagated the uncertainties in fitted parameters to the summed fluxes and hence ratios using Monte Carlo techniques.

To estimate densities from the line ratios, we have performed calculations using CLOUDY v17 (Ferland et al. 2017). We calculated a grid of photoionization models covering a large range in ionization parameter and hydrogen density, with details and assumptions similar to those presented in appendix A of Baron & Netzer (2019). We adopted a standard AGN spectral energy distribution (SED) with a mean energy of an ionizing photon of 2.56 Ryd (SED 2 in table A1 of Baron & Netzer 2019; see also Netzer 2013), although we note that the shape of the ionizing SED has a negligible effect on our conclusions in this section. The assumed metallicity, on the other hand, has a significant effect on the derived densities, which vary by a factor of 2–3 for a metallicity range of 0.5–2 times solar. We present in Section 4.5 evidence that the metallicity is close to solar, and thus we assume solar metallicity. We considered a model grid with seven values of $\log n_H$ in the range 2.0–5.0, and examined eight values for ionization parameter U ranging from -3.8 to -2. The separate grids in ionization parameters were created to match those calculated for our AGN (see Section 4.3 and Table 4), which were derived from the [O III]/Hβ and [N II]/Hα ratios as described in Section 4.3 following Baron & Netzer (2019). Finally, we adopted the extinction law of Cardelli, Clayton & Mathis (1989), taking $A_V = 3.1\,E(B-V)$ and assuming the dust is in a foreground screen. The photoionization models we consider are dusty, and thus dust is also mixed with the ionized gas (see Baron & Netzer 2019 for additional details). However, its effect is taken into account internally within the models (we use *emergent* line luminosities), and thus we do not need to account for it separately. In addition, the column density of the internal dust is small compared to the column derived for the dusty screen in our sources. Two of the resulting model grids are shown in Fig. 7, for $\log U = -2.5$ and -3.5, representing the range of U we find for the individual AGN. The location of our AGN with respect to these models is shown in Fig. 7, and the implied n_e and A_V are given in Table 3. The median density is $n_e = 1900$ cm^{-3} and the 1σ range covers 1200–3000 cm^{-3}, significantly higher than that derived with the *doublet* method.

As a consistency check of our photoionization modelling, we compare the resulting extinction to that derived from the Hα and Hβ lines, assuming an intrinsic ratio Hα/Hβ = 3.1 appropriate for the narrow-line region and using the Cardelli et al. (1989) extinction curves as above (and taking into account the BLR as described in Section 2.4). The resulting extinction, in the range 1–3 mag, is compared in Fig. 8. Here, the dashed line indicates a 1:1 ratio, while the dotted lines are offset by 0.5 mag each. The values from the two methods are comparable to within about 0.5 mag, providing support for our derivation of n_e and A_V from the [O II] and [S II] ratios.

4.3 Ionization parameter method

The *logU* method was proposed by Baron & Netzer (2019) and is based on the definition of the ionization parameter, the number of ionizing photons per atom, $U = Q_{Lyc}/4\pi r^2\, c\, n_H$, where Q_{Lyc} is the ionizing photon rate from a source, r is the distance from that source, and $n_e \sim n_H$ is the local number density of atoms or equivalently electrons. The speed of light, c, is included to make the parameter dimensionless. These authors showed that one can rearrange this to give the electron density n_e in terms of the AGN luminosity, the distance from the AGN, and the ionization parameter such that $n_H \propto L_{AGN}\, r^{-2}\, U^{-1}$. At the same time, they showed that U can be derived rather reliably (i.e. with a scatter of 0.1 dex) from the strong line ratios [N II]/Hα and [O III]/Hβ. That these lines are readily measurable for many AGN makes the method widely applicable. A similar approach was adopted by Revalski et al. (2018a,b) when fitting multiple components with different densities to a suite of line ratios in spatially resolved data for Mrk 573 and Mrk 34, with the difference that they left U as a free parameter and derived it as part of the fit.

For our sample, the absorption corrected 14–195 keV luminosity has been calculated by Ricci et al. (2017) based on 0.3–150 keV broad-band X-ray data. Taking those values, adjusted to our adopted distances, we have used the relation in Winter et al. (2012) to recover the AGN bolometric luminosity. Uncertainties due to the AGN luminosity and this relation, which combine to be about 0.14 dex, will propagate directly into the derived density; but errors in the distance to the source do not affect the derived density because the impact when converting flux to luminosity for L_{AGN} is cancelled

Table 3. Measurements of the [S II] and [O II] line ratios used by the auroral/transauroral method, and derived densities and extinctions for active galaxies.

Object	log [S II] ratio (4069+4076)/(6716+6731)	log [O II] ratio (3726+3729)/(7320+7331)	log n_e (cm^{-3})	A_V (mag)
ESO 137-G034	-1.43 ± 0.01	0.76 ± 0.02	3.13 ± 0.02	1.52 ± 0.04
MCG-05-23-016	-1.01 ± 0.02	0.88 ± 0.02	3.46 ± 0.02	0.55 ± 0.04
NGC 2110	-1.28 ± 0.01	0.36 ± 0.01	3.61 ± 0.02	2.05 ± 0.03
NGC 2992	-1.48 ± 0.02	0.31 ± 0.03	3.43 ± 0.03	2.37 ± 0.06
NGC 3081	-1.31 ± 0.02	1.05 ± 0.01	3.01 ± 0.02	0.82 ± 0.04
NGC 5506	-1.43 ± 0.03	0.61 ± 0.02	3.27 ± 0.03	1.84 ± 0.05
NGC 5728	-1.35 ± 0.03	0.83 ± 0.02	3.16 ± 0.04	1.26 ± 0.06
NGC 7582	-1.36 ± 0.04	0.78 ± 0.05	3.28 ± 0.05	1.57 ± 0.11

Note. Quoted uncertainties are from formal error propagation based on the random noise in the spectrum.

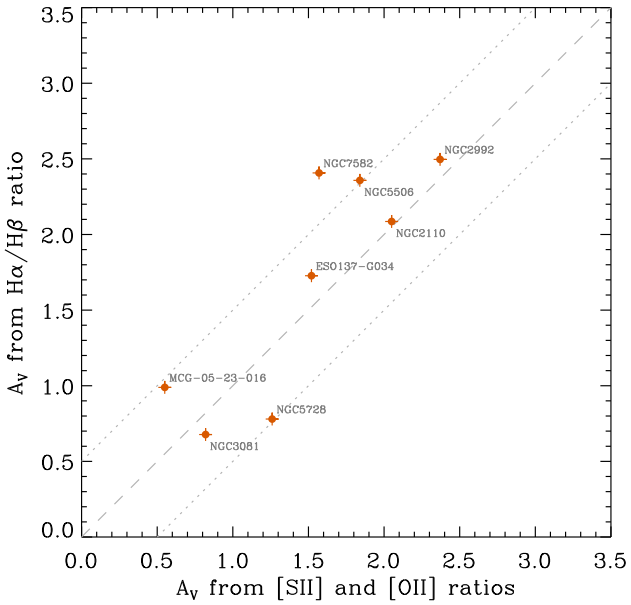

Figure 8. Comparison of extinction A_V derived from the [S II] and [O II] line ratios to that derived from the Hα/Hβ ratio. The dashed line indicates a 1:1 ratio and the dotted lines a $\pm$0.5 mag range.

by the $1/r^2$ term when converting aperture size from arcseconds to parsecs. We have already shown the line ratios in Fig. 2, and we report their values in Table 4.[1] Also given in Table 4 is log U, derived using the equations in Baron & Netzer (2019). The final parameter is the distance r from the AGN. It is clear that this method is most suited to spatially resolved data, where one can take a measurement at a known projected distance from the AGN. In our case, we have only an aperture centred on the AGN, and the luminosity distribution within this can be complex. For the purposes of this analysis, we aim to estimate a reasonable upper limit to r that will therefore lead to an estimate of n_e that is towards the lower end of the likely range. As the projected radius we therefore take the distance of 0.9 arcsec from the centre to the edge of the aperture, which typically corresponds to $\sim$150 pc (this yields r a factor of 1.3 higher than it would be under the assumption of a uniform luminosity distribution). To account for the projection effects, we note that the AGN are Seyfert 2 (see Table 1), and hence oriented more towards edge-on than face-on. For those objects in our sample for which the orientation of the ionized outflow has been estimated, it lies in the range 10°–49° for the Sy 2s from edge-on, and a slightly higher 55° for the Sy 1.8 (Hjelm & Lindblad 1996; Friedrich et al. 2010; Müller-Sánchez et al. 2011; Fischer et al. 2013; Shimizu et al. 2019). We therefore adopt an inclination of 45° from edge-on (this yields r a factor of 1.4 higher than it would be for a fully edge-on outflow). We emphasize that in both cases, uncertainties are likely to be towards smaller values of r and hence higher values for n_e than those we derive (specifically, a reasonable range for n_e would include values a factor of 3–4 higher, but not lower). The resulting densities are reported in Table 4. They have a median value of 4800 cm^{-3} and a 1σ range of 1050–22 000 cm^{-3}. Given the large scatter in values, this is consistent with that found using the *TA* method, and again much higher than that derived with the *doublet* method. It is likely that the scatter is a combination of the uncertainty of the AGN luminosity together with an observational effect related to our use of aperture measurements within which the characteristic distance from the AGN to the line emitting gas is not known. The aperture effect is not a limitation of the method itself, but the impact of the way we apply it here. It creates an uncertainty that is much more acute than for spatially resolved data, and simply means that here we should make use of the derived densities in a statistical sense rather than focussing on individual values.

[1]These differ from those reported in Burtscher et al. (in preparation) by typically <10 per cent, which is attributable to the different resolution and use of single versus multiple Gaussian profiles adopted.

4.4 Comparison of densities

The distributions in Fig. 9 show that the electron densities derived for the three methods cover 1σ ranges of: 210–580 cm^{-3} for the *doublet* method, 1200–3000 cm^{-3} for the *TA* method, and 1050–22 000 cm^{-3} for the *logU* method. The densities from both the *TA* and *logU* methods are consistent, although the scatter of the latter is somewhat larger as discussed above. Both are significantly higher than the densities found with the *doublet* method. The reason for this difference cannot be due to saturation of the [S II] ratio at high densities, because the ratio is not close to its asymptotic limit; nor is it due to blending of the line profiles because our data are both high resolution and high signal-to-noise ratio. Instead, it is related to the physics of the photoionization. It has been known for a long time that the hard radiation field from an AGN produces photons that can penetrate deep into clouds, leading to a partially ionized zone (Osterbrock 1989). This is much more extensive than in gas photoionized by OB stars, and is responsible for the excess emission from low excitation transitions seen in AGN spectra (which lead Veilleux & Osterbrock 1987 to propose the use of species such as [S II], in terms of its flux ratio with respect to Hα, as a diagnostic for AGN). Baron & Netzer (2019) pointed out that because the electron

Table 4. Measurements of the Hα and Hβ fluxes, the [N II]/Hα and [O III]/Hβ line ratios, and the derived ionization parameters and densities for active galaxies.

Object	$F_{H\alpha}$ (10^{-15} erg s^{-1} cm^{-2})	$F_{H\beta}$ (10^{-15} erg s^{-1} cm^{-2})	A_V (Hα/Hβ) (mag)	log [N II]/Hα	log [O III]/Hβ	log U^a (cm^{-3})	log $n_e{}^b$ (cm^{-3})
ESO 137-G034	49.4 ± 0.6	9.25 ± 0.13	1.7	0.044 ± 0.005	1.091 ± 0.006	−2.64 ± 0.10	2.86 ± 0.14
MCG-05-23-016	6.8 ± 0.1	1.60 ± 0.02	1.0	−0.043 ± 0.005	1.112 ± 0.006	−2.58 ± 0.10	3.68 ± 0.14
NGC 2110	41.1 ± 0.5	7.85 ± 0.10	1.7	0.138 ± 0.005	0.678 ± 0.005	−3.31 ± 0.10	4.63 ± 0.14
NGC 2992	10.2 ± 0.2	1.45 ± 0.07	2.5	0.021 ± 0.005	1.067 ± 0.002	−2.68 ± 0.11	2.78 ± 0.16
NGC 3081	68.2 ± 0.2	17.8 ± 0.4	0.7	−0.035 ± 0.001	1.117 ± 0.010	−2.57 ± 0.10	3.49 ± 0.14
NGC 5506	173 ± 45	26.3 ± 0.5	2.4	−0.052 ± 0.118	0.948 ± 0.008	−2.87 ± 0.12	4.03 ± 0.14
NGC 5728	41.8 ± 1.8	10.4 ± 0.3	0.8	0.144 ± 0.018	1.114 ± 0.011	−2.62 ± 0.10	3.48 ± 0.14
NGC 7582	60.9 ± 0.3	9.39 ± 0.08	2.3	−0.173 ± 0.002	0.362 ± 0.003	−3.54 ± 0.10	4.83 ± 0.16
ESO 021-G004	0.7 ± 0.03	0.09 ± 0.01	3.1	0.532 ± 0.019	0.886 ± 0.046	−3.02 ± 0.12	3.10 ± 0.28
NGC 1365	2.7 ± 0.04	0.51 ± 0.01	1.7	0.006 ± 0.006	0.707 ± 0.010	−3.24 ± 0.10	3.70 ± 0.18
NGC 7172	3.1 ± 0.06	0.36 ± 0.02	3.2	0.087 ± 0.008	0.799 ± 0.019	−3.14 ± 0.10	4.01 ± 0.14

Notes. Quoted uncertainties of line fluxes and ratios are from formal error propagation and based on the random noise in the spectrum.
[a]Uncertainty in log U is dominated by the 0.1 dex scatter around the relation with line luminosity in Baron & Netzer (2019).
[b]Uncertainty of log n_e includes that of the 14–195 keV luminosity and 0.09 dex due to the relation between the 14–195 keV and bolometric luminosities given in Winter et al. (2012).

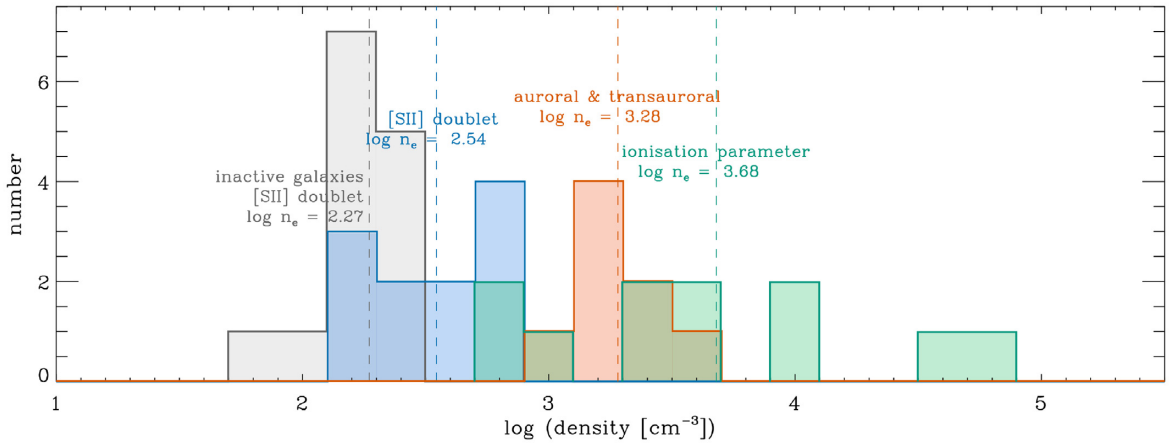

Figure 9. Comparison of the densities measured for the AGN using the different methods: [S II] doublet ratio (blue), using the auroral and transauroral [S II] and [O II] line ratios (red), and based on the ionization parameter (green). In addition, the inactive galaxies, for which the [S II] doublet method was used, are shown in grey. For the doublet and *TA* methods, sample spread dominates over individual measurement errors. Although the *TA* and *logU* methods measure n_H, in fully ionized gas this is the same as n_e. We have therefore labelled median values for all the methods as electron densities.

density decreases further into the cloud, different excitation states of species arise from different regions within the cloud, specifically that while the Hα and [O III] are emitted throughout most of the ionized cloud, much of the [S II] is emitted close behind the ionization front where the electron density drops dramatically. Because the ionization fraction falls rapidly below 10 per cent, most of the gas in this region is neutral.

To illustrate this point, Fig. 10 shows several results from the photoionization models. In the left-hand panel, we show the ionized fraction of hydrogen, oxygen, and sulphur, for a model with log $U = -3$ and log $n_H = 3$, as a function of depth into the cloud. One can see that both H^+ and O^{++}, which are responsible for Hα and [O III] emission, respectively, peak within the ionized cloud. On the other hand, S^+, which is responsible for the [S II] emission, peaks after the ionization front where more than half of the hydrogen is already neutral. In the middle panel, we compare the cumulative line emission of Hα, [O III], and [S II], and show the electron density as a function of depth into the cloud. The Hα and [O III] line luminosities saturate near the ionization front, and one can see that their emission traces high electron density of $n_e \sim 10^3 = n_H$. On the other hand, the [S II] emission extends far into the neutral part of the cloud, reaching 80 per cent of the cumulative line luminosity where the electron density has already dropped by a factor of four. Similar trends are also observed in models with different ionization parameters.

In the right-hand panel of Fig. 10 we compare the electron densities derived using the *TA*, *logU*, and *doublet* methods in our models with log $U = -3$. To estimate the electron densities, we calculate the line luminosities predicted by the models and use the respective ratios discussed in Sections 4.1–4.3 to estimate the electron densities, in order to match our observational approach. The electron densities derived using the *TA* and *logU* methods are similar in all the models we examined, regardless of the ionization parameter. This is expected since both methods trace the hydrogen density in the cloud, which is assumed to be constant in our models. We find a significant difference between the electron densities derived using either of those methods, and those derived using the *doublet* method. This difference increases as the hydrogen density in the cloud increases, and becomes significant even below the critical density $n_H \sim 10^4$ cm^{-3} of the [S II] lines. This is because, independent of the hydrogen density, the [S II] lines trace low electron density regions within the ionized cloud. We therefore suggest that the *doublet*-based electron densities provide a biased view of the ionized cloud, and that they should not be used

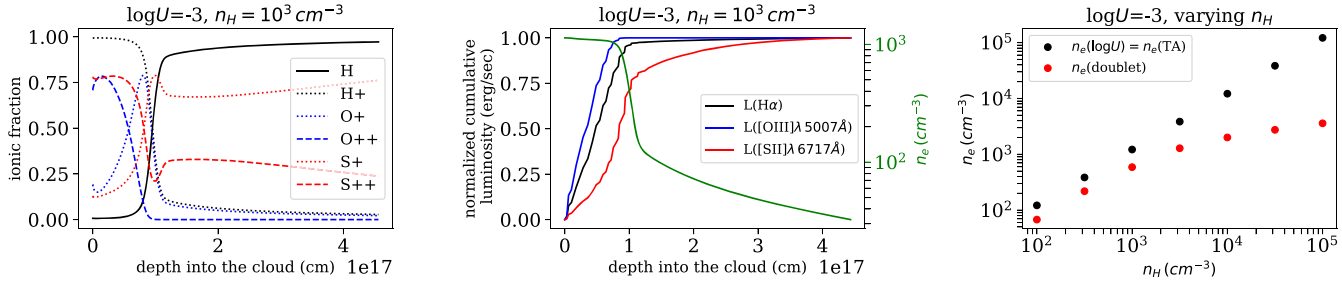

Figure 10. Photoionization model showing how different emission lines trace different properties of a constant density cloud (see Baron & Netzer 2019 for details of the models). Left: relative population of various ions as a function of distance into the cloud. One can define the ionization front to be where most of the hydrogen is neutral. Centre: resulting line emission, and also electron density, as a function of depth into the cloud. This shows that much of the [S II] line originates from mostly neutral gas where the electron density is lower. Right: comparison of electron density as measured from the model using the methods described in the text, as a function of hydrogen density in the cloud. At $n_e > 10^3$ cm^{-3} the discrepancy between the density derived from the [S II] doublet ratio and that found using the other methods (which trace the actual density) is significant.

above $n_e \sim 10^3$ cm^{-3}, since then the hydrogen density (and thus the electron density in the ionized part of the cloud) can be a factor of 3–100 larger. This invalidates key assumptions in the use of the [S II] doublet to estimate the density of the ionized cloud, and thus its mass.

4.5 Ionized gas masses

As noted in Section 1, given a particular transition with volume emissivity $\gamma_{\rm line}$ and emission line luminosity $L_{\rm line}$, the ionized gas mass can be estimated using $M_{\rm ion} = \mu m_{\rm H}\, L_{\rm line}/(\gamma_{\rm line}\, n_e)$, where n_e is the electron density in the *line-emitting* region. The volume emissivity, $\gamma_{\rm line}$, depends on known atomic physics and on the physical properties of the cloud (for additional details see Baron & Netzer 2019). We have demonstrated in Section 4.4 that different emission lines are emitted in different parts of the ionized cloud, with those regions showing significantly different electron densities and temperatures. Therefore, the common practice of estimating the ionized gas mass using $L_{\rm H\alpha}$ or $L_{\rm [O\,III]}$ and an electron density from the [S II] doublet is invalid and will result in an overestimate of the ionized gas mass. As first argued by Baron & Netzer (2019), it is necessary to use density tracers that match the emission line in question in order to obtain an unbiased estimate of the gas mass in the cloud. For example, when using $L_{\rm H\alpha}$ or $L_{\rm [O\,III]}$, it is necessary to use *TA*- or *logU*-based electron densities; when estimating the ionized gas mass using the *doublet*-based density, it is necessary to use the [S II] luminosity (although with an additional caveat described below about the valid density range). Mixing these up would result in an incorrect estimate of the ionized gas mass.

Baron & Netzer (2019) calculated the effective line emissivities for the Hα and [O III] emission lines, by taking the mean emissivity in the cloud weighted by the electron density. Since, in those models, the Hα and [O III] lines are emitted in similar regions within the ionized cloud, the effective emissivities are expected to result in similar masses when using either the Hα or [O III] emission lines. However, if two transitions are emitted in different regions within the cloud, we no longer expect their masses to be equal to each other, even when using the appropriate effective emissivities and electron densities. This is because the mass of the gas that emits the different transitions may be different. For the example in Fig. 10, the mass of the [S II]-emitting gas is roughly a factor of 2 larger than the mass in the Hα-emitting region. More generally we find that, for $n_e \lesssim 10^3$ cm^{-3}, the gas mass ratio of the [S II]- and Hα-emitting regions is 1–3, depending on the ionization parameter.

Table 5. Effective emissivities.

log U	$\gamma_{\rm eff}{}^a$ (10^{-25} cm^3 erg s^{-1})		
	Hα	[S II] 6716 Å^b	[O III] 5007 Å
−2.00	1.75	0.46	7.03
−2.26	2.02	0.58	7.41
−2.51	2.25	0.79	7.19
−2.77	2.45	1.13	6.35
−3.03	2.57	1.60	4.81
−3.29	2.53	2.12	2.87
−3.54	2.55	2.86	1.33
−3.80	2.26	3.17	0.41

[a]See Section 4.5 for an explanation of how these were calculated.
[b]The values for [S II] emissivity are only valid for $n_e < 10^3$ cm^{-3}.

In this work, our goal is to calculate effective line emissivities for the Hα, [O III], and [S II] emission lines, that will result in *similar* ionized gas masses. To achieve this, it is necessary to scale each of the emissivities so that the mass traced by the different transitions is similar. We begin by defining an effective electron density $\langle n_e \rangle_{\rm line}$ as the luminosity-weighted mean electron density in the cloud. Its value will depend on the emission line used, and is a reasonable approximation to the values that would be derived observationally using the methods discussed in Sections 4.1–4.3. We define the ionization front, separating the fully ionized and mostly neutral regions of the cloud, to be where 80 per cent of the hydrogen is neutral.[2] Defining the ionized gas mass $M_{\rm ion}$ to be the mass of the gas before the ionization front, we calculate the effective product $\langle \gamma_{\rm line} n_e \rangle = \mu m_{\rm H}\, L_{\rm line}/M_{\rm ion}$ using the integrated line luminosity $L_{\rm line}$ for each of the three emission lines Hα, [O III], and [S II]. We can then define the new effective emissivities as $\langle \gamma_{\rm line} \rangle = \langle \gamma_{\rm line} n_e \rangle / \langle n_e \rangle_{\rm line}$. Values for $\langle \gamma_{\rm line} \rangle$ for Hα, [O III], and [S II] are given in Table 5 as a function of log U. It is notable in this table that even $\gamma_{\rm H\alpha}$ is rather different from its canonical value of 3.6×10^{-25} cm^3 erg s^{-1} (Osterbrock 1989). By construction, $\langle \gamma_{\rm line} \rangle$ will yield a similar mass for the ionized gas independent of which tracer is used, as long as one uses the matching estimate of electron density. Our constant density models verify the efficacy of this approach to 10–20 per cent.

Fig. 11 compares the ionized masses derived using this technique for our AGN sample. The far left-hand panel shows we find a

[2]The exact definition of the ionization front (i.e. where the 50, 80, or 90 per cent of the hydrogen is neutral) has a negligible effect on the resulting ionized gas mass.

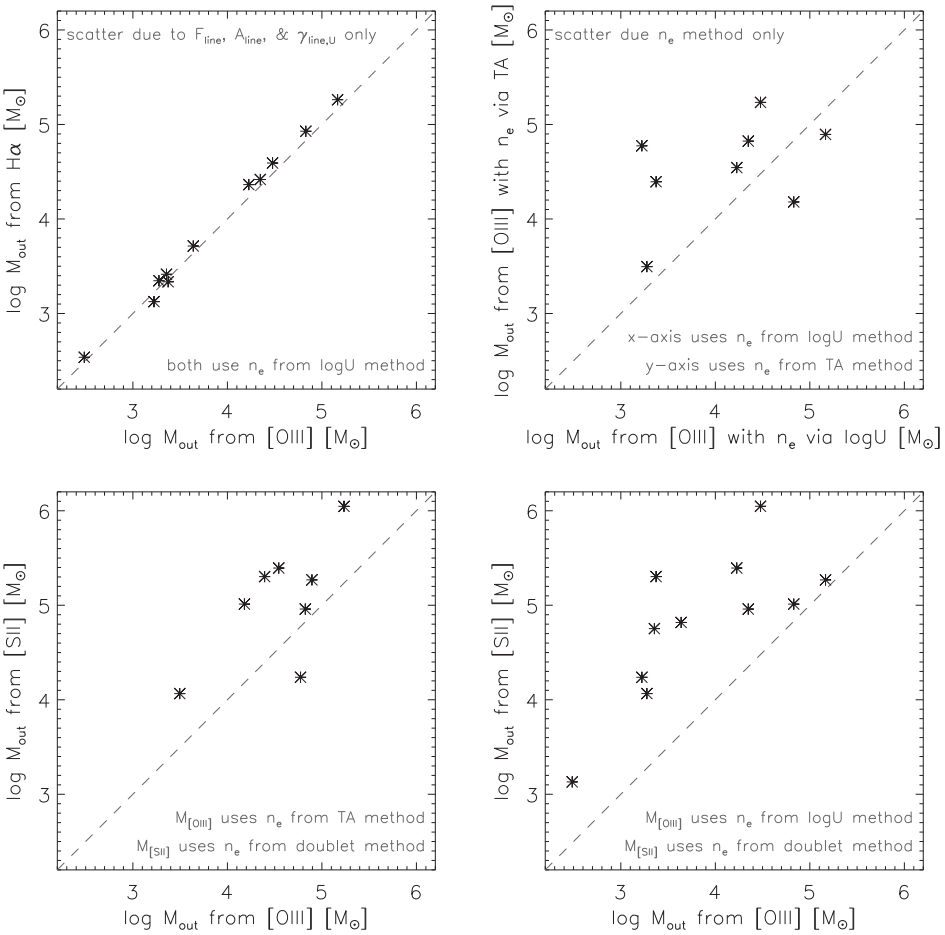

Figure 11. Comparison of the derived masses using different tracers and density estimates. Top left: when using the same n_e method, the masses from the Hα line and [O III] line are very similar. Top right: when using the same line, the masses using n_e from the *logU* and *TA* methods scatter around a 1:1 line. Bottom: an offset is found for the masses derived from the [S II] line with n_e from the *doublet* method, and the [O III] line with n_e from the *TA* (left) or *logU* (right) method. This offset is consistent with the rapid increase in discrepancy for the *doublet* method at $n_e > 10^3$ cm^{-3}, where our calculation of $\gamma_{[S\,II]}$ is no longer valid. See the text for a discussion of these panels.

negligible (<0.1 dex) difference in mass when using $L_{H\alpha}$ or $L_{[O\,III]}$. Since these were both calculated using the same density tracer, it is a verification of our measurements and our approach to calculating γ_{eff}. It also acts as a posteriori support for adopting solar metallicity. The centre left-hand panel compares the *TA* and *logU* methods for the same line. Since our models indicate that these should yield the same density, the modest difference is likely due to a systematic effect in AGN luminosity or adopted distance from the AGN to the line emission, or due to complexities that our constant density models do not address. The centre right-hand panel shows a factor of 3 difference between using the [O III] line with the *TA* method, and the [S II] line with the *doublet* method. The former is more robust, and as indicated in the right-hand panel of Fig. 10, the difference between this and the [S II] derived mass is a further indication that $n_e > 10^3$ cm^{-3} where our calculated $\gamma_{[S\,II]}$ can no longer be properly applied. Similarly, the far right-hand panel compares the [O III] line and *logU* method with the [S II] line and *doublet* method.

Our summary for these three density estimators is then: the *doublet* method is severely biased. It will yield incorrect masses unless used with the [S II] line luminosity and $\gamma_{[S\,II]}$ given in Table 5; and even then it can only be used when $n_e < 10^3$ cm^{-3}. The *TA* method is robust, but unfortunately in many cases impractical because it relies on measurements of very weak lines. Even in our sample of local luminous AGN we were unable to use it in about 1/3 of the cases. The *logU* method is both robust and straightforward to apply. It has the additional advantage of emphasizing, by its definition, that the density is expected to decrease at increasing distance from the AGN. It is, however, more suited to spatially resolved data and one needs to be careful when estimating the characteristic distance from the AGN to the outflow in aperture measurements. It is this method together with the [O III] line luminosity and respective emissivity that we use in Section 5 when estimating the outflow rates for the AGN.

5 OUTFLOW MASS AND RATE

The expression for the outflow rate $\dot{M}_{out}$ depends on the outflow scenario and geometry considered (see e.g. Lutz et al. 2020). One option is to assume a spherically or biconically symmetric flow with constant velocity and uniform density up to a given radius (e.g. Cano-Díaz et al. 2012; Brusa et al. 2015; Bischetti et al. 2017; Fiore et al. 2017; Rojas et al. 2020). In this scenario, the outflow rate decreases over time, and what one calculates is the initial outflow rate that is traced by the material at the maximum radius considered. The outflow rate is then a factor of 3 higher than that derived using the common alternative models of a time-averaged thin shell geometry, or a density profile scaling as r^{-2} so that the outflow rate is constant

Table 6. Measured and derived properties related to outflows in the active galaxies.[a]

Object	$\log L_{\rm AGN}$ (erg s^{-1})	$R_{\rm ap}$ [b] (pc)	$\log L_{[\rm O\,III]}$ (erg s^{-1})	$v_{98,[\rm O\,III]}$ (km s^{-1})	$\log M_{\rm out}$ [c] ($M_\odot$)	$\dot{M}$ ($M_\odot$ yr^{-1})	$\dot{E}_{\rm kin}$ (erg s^{-1})	$\log \dot{E}_{\rm kin}/L_{\rm AGN}$
ESO 137-G034	43.4	152	40.8	519	5.2	0.52	40.7	− 2.7
MCG-05-23-016	44.3	152	39.7	255	3.3	0.003	37.8	− 6.4
NGC 2110	44.5	148	40.4	1665	3.4	0.03	40.4	− 4.1
NGC 2992	43.3	157	40.4	587	4.8	0.26	40.5	− 2.8
NGC 3081	44.1	148	40.6	279	4.3	0.04	39.0	− 5.0
NGC 5506	44.1	117	41.2	792	4.5	0.21	40.6	− 3.5
NGC 5728	44.1	170	40.5	876	4.2	0.09	40.3	− 3.8
NGC 7582	44.0	95	40.1	364	3.2	0.007	38.4	− 5.6
ESO 021-G004	43.3	170	39.4	432	3.6	0.01	38.8	− 4.5
NGC 1365	43.0	78	38.6	373	2.5	0.002	37.8	− 5.2
NGC 7172	44.1	161	39.9	397	3.3	0.005	38.4	− 5.7

[a]As discussed in Section 4.4, we have adopted $n_{\rm e}$ derived using the *logU* method. As such, the uncertainty of $M_{\rm out}$ is dominated by the uncertainty of $n_{\rm e}$ that is typically 0.14 dex (through $\log U$ and $L_{\rm AGN}$). This propagates directly into the outflow rate $\dot{M}$ and kinetic power $\dot{E}_{\rm kin}$ (for both of which the choice of outflow model can have a factor of 3 impact). Because $L_{\rm AGN}$ impacts the ratio $\dot{E}_{\rm kin}/L_{\rm AGN}$ a second time, the uncertainty on that increases to 0.21 dex.
[b]The radius of the outflow $r_{\rm out}$ is based on the aperture radius $R_{\rm ap}$ with an adjustment for projection as described in Section 4.3.
[c]For consistency with our use of $L_{[\rm O\,III]}$, we have used $v_{98,[\rm O\,III]}$ rather than $v_{98,[\rm S\,II]}$, although typically they differ by only ∼25 per cent.

over time. (e.g. Rupke, Veilleux & Sander 2005c; González-Alfonso et al. 2017; Veilleux et al. 2017; Fluetsch et al. 2019; Lutz et al. 2020). We have adopted the latter class of models, for which $\dot{M}_{\rm out} = M_{\rm out}\, v_{\rm out}/r_{\rm out}$ Similarly the kinetic power of the outflow is calculated as $\dot{E}_{\rm kin} = 1/2\, \dot{M}_{\rm out}\, v_{\rm out}^2$.

We have used the [O III] line luminosity when calculating the outflowing mass, and adopted the volume emissivity $\gamma_{[\rm O\,III]}$ given in Table 5. To be consistent with that, we have also used the maximum outflow velocity derived from the [O III] line, $v_{98,[\rm O\,III]}$. In terms of $n_{\rm e}$, we have taken that derived using the *logU* method. The resulting outflowing masses and rates are given in Table 6. We note that if we were to use the Hα line luminosity to estimate mass, with $\gamma_{\rm H\alpha}$ as given in Table 5, we would get very similar outflowing masses as is shown in the left-hand panel of Fig. 11; and if we were to use $v_{98,[\rm S\,II]}$ as the outflow velocity, the left-hand panel of Fig. 3 shows that the outflow rates would be about 25 per cent lower. As a cross-check, we compare the outflow rates for two objects to recently published values based on spatially resolved data. Despite the different methods used, our outflow rate for NGC 5728 compares well to that of 0.08 $M_\odot$ yr^{-1} for both sides of the outflow within 250 pc found by Shimizu et al. (2019). For NGC 1365, the outflow rate on the south-east side within 380 pc found by Venturi et al. (2018) was 0.01 $M_\odot$ yr^{-1}. This is about a factor of 10 higher than ours because, as discussed above, the density from the [S II] doublet used by those authors, leads to an overestimate of the outflowing mass by that amount.

5.1 Outflow rate relation at low luminosity

Although the AGN in our sample are considered luminous with respect to local AGN, they are of only moderate luminosity when compared to samples taken from larger distances that include luminous quasars. As such, they provide an opportunity to extend to lower luminosity the relation between AGN luminosity and outflow rate in the literature. One of the most well known is that of Fiore et al. (2017), which is shown in the left-hand panel of Fig. 12. However, there are two important adjustments to our data required in order to affect such a comparison. The first is that Fiore et al. (2017) adopted a definition of outflow rate that is a factor of 3 higher than the one we use above (as discussed at the start of this section). The second is that to deal with the multitude of values for $n_{\rm e}$ adopted in the literature by different authors in the data they compiled, Fiore et al. (2017) rescaled the mass of outflowing gas using a single electron density of $n_{\rm e} = 200$ cm^{-3}. This is a rather problematic issue, because that density is less than any of those we have measured in our AGN sample. To indicate the major impact this has, we have plotted our derived outflow rates from Table 6 as filled circles, and values adjusted to $n_{\rm e} = 200$ cm^{-3} as open circles. It is immediately clear that the relatively low scatter in the relation over five orders of magnitude is at least partly due to the adoption of a single value for the density of all the outflows. Using the densities we have derived, the low-luminosity AGN are highly scattered and lie below where one would expect from the correlation.

Addressing this issue has prompted us to look also at the parameters $L_{\rm line}$ and $v_{\rm out}$ that contribute to the relation given that, for constant $n_{\rm e}$, $\dot{M}_{\rm out} \propto L_{\rm line}\, v_{\rm out}/r_{\rm out}$ as shown in Section 1 (and noting that there is no individual correlation between $L_{\rm AGN}$ and $r_{\rm out}$). Using the data in Fiore et al. (2017), we have calculated (by 'reverse engineering') the effective [O III] luminosity $L_{[\rm O\,III],\rm eff}$ that would be required to produce the given outflow rate, and have verified this approach using the [O III] luminosities available (Fiore, private communication). The individual correlations for $L_{[\rm O\,III],\rm eff}$ and $v_{\rm out}$ are shown in the centre and right-hand panels of Fig. 12. They show that it is the line luminosity $L_{[\rm O\,III]}$ rather than the outflow speed $v_{\rm out}$ that must be the primary driver of the correlation over so many orders of magnitude. It is a long established relation for X-ray-selected AGN (Mulchaey, Koratkar & Ward 1994; Alonso-Herrero, Ward & Kotilainen 1997; Heckman & Best 2014), which has a similar large scatter. Using a sample selected on the basis of broad Hα, Stern & Laor (2012) find a good (approximately linear) correlation with a scatter of 0.44 dex; and based on compiled data for a very hard X-ray selected sample, Berney et al. (2015) suggest that the scatter is 0.62 dex. The scatter for the Fiore et al. (2017) data shown here is 0.67 dex. Although there will be additional uncertainty in our 'reverse engineered' estimate of $L_{[\rm O\,III]}$, the correlation covers the range required, and naturally accounts for the approximate proportionality between $\dot{M}_{\rm out}$ and $L_{\rm AGN}$ – although some authors have noted a non-linear relation between narrow line and AGN luminosity (Netzer et al. 2006; Stern & Laor 2012).

Given the issues above, we explore an alternative representation of the Fiore et al. (2017) relation: instead of fixing a constant density

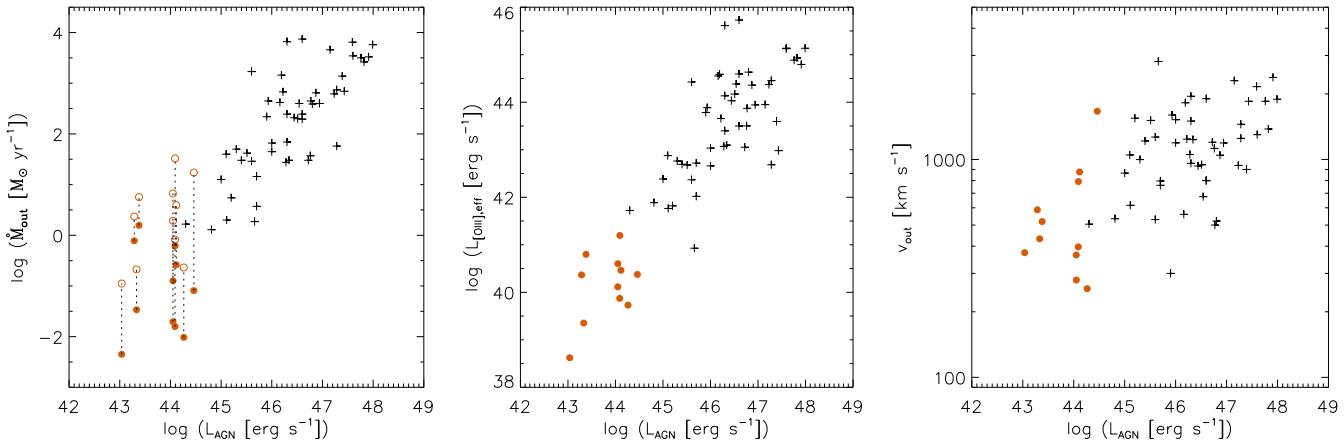

Figure 12. Relations with L_{AGN} using data from Fiore et al. (2017) (black plus points) and from Table 6 for our AGN sample (red filled circles). Left: relation with $\dot{M}_{out}$. In this panel, the outflow rates for our AGN have been increased by a factor of 3 to match the equation used by Fiore et al. (2017). The open circles indicate how those points would shift if in addition we used $n_e = 200$ cm^{-3} as adopted by those authors for all their objects. One needs to be cautious with this relation. Centre: relation with $L_{[O\,III],eff}$, the luminosity that would be required to produce the given outflow rate. This covers five orders of magnitude, and is the primary driver of the outflow rate relation. Right: relation with v_{out} (as given by Fiore et al. 2017, and $v_{98,[O\,III]}$ for our AGN). This covers barely a single order of magnitude and so does not contribute much to the outflow rate relation.

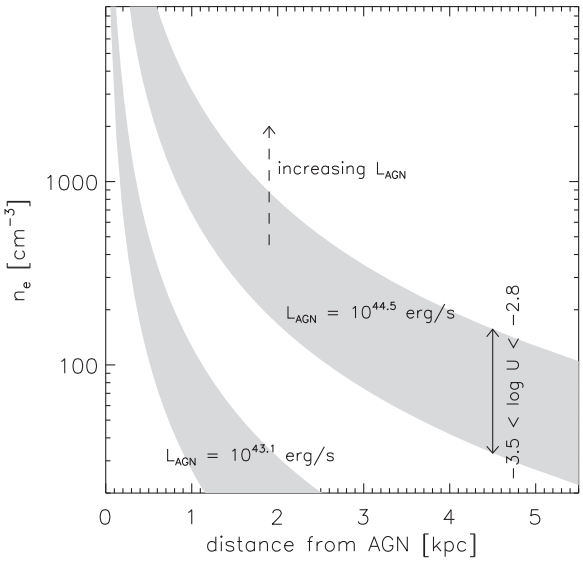

Figure 13. Illustration of how one might estimate a reasonable range for the electron density in an outflow at a given distance from an AGN of known luminosity. This figure shows two example ranges for L_{AGN} corresponding to the minimum and maximum in our sample. The grey regions indicate the uncertainty due to an unknown ionization parameter. This figure should be used as a guide only, and emphasizes how much variation can be expected in outflow densities between objects and at different radii.

for all objects, we adopt an estimate of the density based on the *logU* method. We use the given AGN luminosities L_{AGN} and outflow sizes r_{out}, making the same assumptions as in Section 4.3 about distribution of line luminosity within an aperture and projection. We adopt a value of $\log U = -2.7$, calculated to be the median for the outflows in Fiore et al. (2017) for which both [O III] and Hβ luminosities are available (Fiore, private communication), and which should therefore be characteristic for AGN photoionized outflowing gas. We can then make an order-of-magnitude estimate of n_e as illustrated in Fig. 13. The key point of this figure is that it emphasizes the enormous variation that can be expected for n_e in different outflows. It highlights how in the central few hundred parsecs one can find densities in the range 10^3–10^4 cm^{-3}; and that while in some AGN this may fall to $\sim$100 cm^{-3} at kiloparsec scales, for luminous quasars it may still be in the $\sim$1000 cm^{-3} range.

Bearing in mind the expected variation in outflow density, in Fig. 14 we have modified the relation of Fiore et al. (2017) to take into account our best estimate of n_e for the individual objects, and overplotted both our data and data from Baron & Netzer (2019). The relation between AGN luminosity and outflow rate, which covers five orders of magnitude in L_{AGN}, remains but with two important differences: (i) the scatter is much larger than before, and (ii) the outflow rates are typically lower by about a factor of 3 since the densities are generally that much higher. The original relation appears to be more of an upper limit on the outflow rate, but not all AGN-driven outflows reach that limit. With the data available, the values we have estimated for n_e are still uncertain and so we would only claim that this modified relation should be considered as equally valid as the original relation of Fiore et al. (2017). It does, however, underline that there remain unanswered questions about how the ionized gas outflow rate is related to AGN luminosity.

6 CONCLUSION

We present an analysis of the kinematics and electron density derived from emission lines integrated over the central 1.8 arcsec ($\sim$300 pc) of local luminous active galaxies and matched inactive galaxies. The data are from X-shooter observations, taken as part of the LLAMA survey, which comprises a complete volume-limited sample of 14–195 keV selected AGN together with inactive galaxies matched by their global properties. Our findings are as follows.

(i) The peak of the emission lines in the AGN is offset from systemic (traced by stellar absorption features), indicating that the line profiles of the AGN are dominated by outflow. Any systemic component is highly subdominant. In contrast, the line profiles of the inactive galaxies are characterized by a core close to the systemic velocity with a wing tracing outflow.

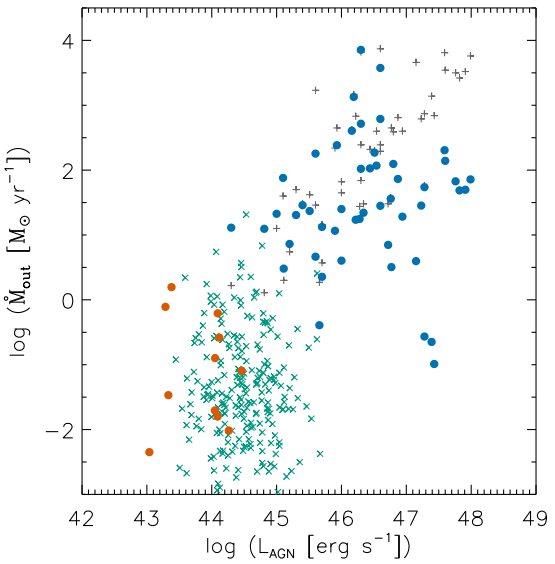

Figure 14. A modification to the well-known relation from Fiore et al. (2017) in which we have adjusted the outflow rates according to our best estimate of the density as described in Section 5.1. The original data are shown as grey plus points, while the adjusted points are drawn as filled blue circles. We have included our own points as filled red circles (again a factor of 3 more than in Table 6, as described in Section 5.1), as well as the data from Baron & Netzer (2019) as green crosses. A correlation remains but there is more scatter than before, and with the original data tracing its upper limit. The three outliers at high L_{AGN} and low $\dot{M}$ are at $z \sim 2.4$. One was already a low point on the original relation; the other two have very high estimated densities because r_{out} is small.

(ii) For the galaxies with weak emission lines (equivalent width of [S II] 6716 Å $\lesssim$10 Å), the [S II] doublet ratio method overestimates the electron density unless a correction is made for stellar absorption features. This is particularly important for the inactive galaxies where the impact on n_e is a factor of 2. After correcting for the stellar continuum, their median density is found to be $n_e = 190$ cm^{-3}.

(iii) For the active galaxies, the densities found using three independent methods (the [S II] doublet ratio, a method using auroral and transauroral line ratios, and a method based on the ionization parameter) differ. The median densities found with these methods are 350, 1900, and 4800 cm^{-3}, respectively. The latter two have comparable ranges and are both significantly larger than the density found with the [S II] doublet ratio. An explanation for this difference lies in the ionization structure of the clouds. Specifically, in the conditions considered here, most of the [S II] line emission originates in a partially ionized zone where n_e drops rapidly to below 10 per cent of n_H and most of the gas is neutral. This invalidates the assumptions under which the [S II] doublet is used to estimate density.

(iv) The definition of 'ionized mass' ought to be treated carefully. Specifically, the extensive region in which most of the gas is neutral increases the total mass of the cloud by a factor of 2–4 with respect to the fully ionized gas.

(v) The implied outflow rates are 0.001–0.5 $M_\odot$ yr^{-1}, and span an order of magnitude more range than the AGN luminosities of (1–30) $\times$ 10^{43} erg s^{-1}. Over this limited range of luminosity, the scatter in outflow rate is the dominant effect, overwhelming the relation between the two quantities.

(vi) The AGN in this sample extend the lower luminosity end of the relation between outflow rate and AGN luminosity in the literature. However, caution needs to be applied when making such comparisons because of uncertainties in the outflow density. Adjusting the data points in the relation using our best estimate of n_e shows that there may be more scatter than previously thought, and that the outflow rates may be at least a factor of a few lower than previously estimated.

ACKNOWLEDGEMENTS

The authors thank the referee for careful reading of the manuscript and providing feedback that helped to improve it. We thank all the staff of the Paranal Observatory who was involved in carrying out the service mode observations used in this paper. We extend particular thanks to Fabrizio Fiore for providing additional data for the ionized outflows. We also thank Marina Trevisan for a discussion about features in the stellar continuum. RR thanks CNPq, CAPES, and FAPERGS. This research has made use of the NASA/IPAC Extragalactic Database (NED), which is funded by the National Aeronautics and Space Administration and operated by the California Institute of Technology.

DATA AVAILABILITY

The data underlying this paper are available in the ESO Science Archive Facility, at http://archive.eso.org/cms.html. The data sets were derived from observations that are in the public domain, under Program ID 095.B-0059(A) and 092.B-0083(A).

REFERENCES

Alonso-Herrero A., Ward M., Kotilainen J., 1997, MNRAS, 288, 977
Bae H.-J., Woo J.-H., 2016, ApJ, 828, 97
Barbuy B., Trevisan J., de Almeida A., 2018, Publ. Astron. Soc. Aust., 35, e046
Baron D., Netzer H., 2019, MNRAS, 486, 4290
Baron D. et al., 2018, MNRAS, 480, 3993
Baron D., Netzer H., Davies R., Prochaska J. X., 2020, MNRAS, 494, 5396
Baumgartner W., Tueller J., Markwardt C., Skinner G., Barthelmy S., Mushotzky R. F., Evans P. A., Gehrels N., 2013, ApJS, 207, 19
Berney S. et al., 2015, MNRAS, 454, 3622
Binggeli B., Sandage A., Tammann G., 1985, AJ, 90, 1681
Bischetti M. et al., 2017, A&A, 598, A122
Brusa M. et al., 2015, MNRAS, 446, 2394
Buta R. J. et al., 2015, ApJS, 217, 32
Caglar T. et al., 2020, A&A, 634, A114
Cano-Díaz M., Maiolino R., Marconi A., Netzer H., Shemmer O., Cresci G., 2012, A&A, 537, L8
Cappellari M., 2017, MNRAS, 466, 798
Cappellari M., Emsellem E., 2004, PASP, 116, 138
Cardelli J., Clayton C., Mathis J., 1989, ApJ, 345, 245
Carniani S. et al., 2015, A&A, 580, A102
Cid Fernandes R., Stasińska G., Schlickmann M., Mateus A., Vale Asari N., Schoell W., Sodré L., Jr, 2010, MNRAS, 403, 1036
Cid Fernandes R., Stasińska G., Mateus A., Vale Asari N., 2011, MNRAS, 413, 1687
Coelho P., 2014, MNRAS, 440, 1027
Davies R. et al., 2015, ApJ, 806, 127
Davies R. et al., 2017, MNRAS, 466, 4917
de Vaucouleurs G., de Vaucouleurs A., Corwin H. G., Jr, Buta R. J., Paturel G., Fouque P., 1991, Third Reference Catalogue of Bright Galaxies. Vol. I: Explanations and References. Vol. II: Data for Galaxies Between 0^h and 12^h. Vol. III: Data for Galaxies Between 12^h and 24^h. Springer, New York
do Nascimento J. C. et al., 2019, MNRAS, 486, 5075
Doyle M. T. et al., 2005, MNRAS, 361, 34
Dressler A., 1984, ApJ, 286, 97
Fabian A., 2012, ARA&A, 50, 455

Ferland G. J. et al., 2017, Rev. Mex. Astron. Astrofis., 53, 385
Fiore F. et al., 2017, A&A, 601, A143
Fischer T., Crenshaw D. M., Kraemer S., Schmitt H., 2013, ApJS, 209, 1
Fischer T. C. et al., 2017, ApJ, 834, 30
Fischer T. C. et al., 2018, ApJ, 856, 102
Fluetsch A. et al., 2019, MNRAS, 483, 4586
Förster Schreiber N. M. et al., 2014, ApJ, 787, 38
Förster Schreiber N. M. et al., 2019, ApJ, 875, 21
Freitas I. C. et al., 2018, MNRAS, 476, 2760
Friedrich S., Davies R., Hicks E., Engel H., Müller-Sánchez F., Genzel R., Tacconi L., 2010, A&A, 519, A79
Gallagher J., Smith L., 1999, MNRAS, 304, 540
González-Alfonso E. et al., 2017, ApJ, 836, 11
Harrison C. M., Alexander D. M., Mullaney J. R., Swinbank A. M., 2014, MNRAS, 441, 3306
Harrison C. M., Costa T., Tadhunter C. N., Flütsch A., Kakkad D., Perna M., Vietri G., 2018, Nat. Astron., 2, 198
Heckman T., Best P., 2014, ARA&A, 52, 589
Hinkle J., Veilleux S., Rupke D., 2019, ApJ, 881, 31
Hjelm M., Lindblad P., 1996, A&A, 305, 727
Hobbs L., 1974, ApJ, 191, 381
Holt J., Tadhunter C., Morganti R., Emonts B., 2011, MNRAS, 410, 1527
Kakkad D. et al., 2016, A&A, 592, A148
Kakkad D. et al., 2018, A&A, 618, A6
Kauffmann G. et al., 2003, MNRAS, 346, 1055
Keel W., 1996, ApJS, 106, 27
Kewley L., Dopita M., Sutherland R., Heisler C., Trevena J., 2001, ApJ, 556, 121
Kewley L., Groves B., Kauffmann G., Heckman T., 2006, MNRAS, 372, 961
King A., Pounds K., 2015, ARA&A, 53, 115
Koss M. et al., 2017, ApJ, 850, 74
Lin M.-Y. et al., 2018, MNRAS, 473, 4582
Liu G., Zakamska N., Greene J., Nesvadba N., Liu X., 2013, MNRAS, 436, 2576
Lutz D. et al., 2020, A&A, 633, A134
Markwardt C. B., 2009, in Bohlender D. A., Durand D., Dowler P., eds, ASP Conf. Ser. Vol. 411, Astronomical Data Analysis Software and Systems XVIII. Astron. Soc. Pac., San Francisco, p. 251
Matt G., Guainazzi M., Maiolino R., 2003, MNRAS, 342, 422
Mendel T., Proctor R., Forbes D., Brough S., 2008, MNRAS, 389, 749
Mingozzi M. et al., 2019, A&A, 622, A146
Modigliani A. et al., 2010, Proc. SPIE, 7737, 773728
Morganti R., 2017, Frontiers Astron. Space Sci., 4, 42
Mulchaey J., Koratkar A., Ward M., 1994, ApJ, 436, 586
Müller-Sánchez F., Prieto M. A., Hicks E., Vives-Arias H., Davies R., Malkan M., Tacconi L., Genzel R., 2011, ApJ, 739, 69
Netzer H., 2013, The Physics and Evolution of Active Galactic Nuclei. Cambridge Univ. Press, Cambridge
Netzer H., Mainieri V., Rosati P., Trakhtenbrot B., 2006, A&A, 453, 525
Osterbrock D. E., 1989, Astrophysics of Gaseous Nebulae and Active Galactic Nuclei. University Science Books, Sausalito, CA
Perna M., Lanzuisi G., Brusa M., Cresci G., Mignoli M., 2017, A&A, 606, A96
Perrotta S., Hamann F., Zakamska N., Alexandroff R., Rupke D., Wylezalek D., 2019, MNRAS, 488, 4126
Pisano D., Barnes D., Staveley-Smith L., Gibson B., Kilborn V., Freeman K., 2011, ApJS, 197, 28
Rajpurohit A. S., Reylé C., Allard F., Scholz R.-D., Homeier D., Schultheis M., Bayo A., 2014, A&A, 564, A90
Revalski M., Crenshaw D., Kraemer S., Fischer T., Schmitt H., Machuca C., 2018a, ApJ, 856, 46
Revalski M. et al., 2018b, ApJ, 867, 88
Ricci C. et al., 2017, ApJS, 233, 17
Riffel R. A., Storchi-Bergmann T., Winge C., 2013, MNRAS, 430, 2249
Riffel R. A., Storchi-Bergmann T., Riffel R., 2015, MNRAS, 451, 3587
Rojas A. F. et al., 2020, MNRAS, 491, 5867
Rosario D. et al., 2018, MNRAS, 473, 5658
Rose M., Tadhunter C., Ramos Almeida C., Rodríguez Zaurín J., Santoro F., Spence R., 2018, MNRAS, 474, 128
Rupke D., Veilleux S., 2011, ApJ, 729, L27
Rupke D., Veilleux S., Sanders D., 2005a, ApJS, 160, 87
Rupke D., Veilleux S., Sanders D., 2005b, ApJ, 632, 751
Rupke D., Veilleux S., Sander D., 2005c, ApJS, 160, 115
Rupke D., Gültekin K., Veilleux S., 2017, ApJ, 850, 40
Santoro F., Rose M., Morganti R., Tadhunter C., Oosterloo T. A., Holt J., 2018, A&A, 617, A139
Schnorr-Müller A., Storchi-Bergmann T., Robinson A., Lena D., Nagar N. M., 2016a, MNRAS, 457, 972
Schnorr-Müller A. et al., 2016b, MNRAS, 462, 3570
Schwartz C., Martin C., 2004, ApJ, 610, 201
Shimizu T. et al., 2019, MNRAS, 490, 5860
Somerville R., Davé R., 2015, ARA&A, 53, 51
Stasińska G. et al., 2008, MNRAS, 391, L29
Stern J., Laor A., 2012, MNRAS, 426, 2703
Storchi-Bergmann T., Simões Lopes R., McGregor P., Riffel R. A., Beck T., Martini P., 2010, MNRAS, 402, 819
Van den Bosch R., Gebhardt K., Gültekin K., Yildirim A., Walsh J., 2015, ApJS, 218, 10
Veilleux S., 1991, ApJ, 369, 331
Veilleux S., Osterbrock D., 1987, ApJS, 63, 295
Veilleux S., Cecil G., Bland-Hawthorn J., 2005, ARA&A, 43, 769
Veilleux S. et al., 2013, ApJ, 776, 27
Veilleux S., Bolatto A., Tombesi F., Meléndez M., Sturm E., González-Alfonso E., Fischer J., Rupke D. S. N., 2017, ApJ, 843, 18
Veilleux S., Maiolino R., Bolatto A., Aalto S., 2020, A&AR, 28, 2
Venturi G. et al., 2018, A&A, 619, A74
Wegner G. et al., 2003, AJ, 126, 2268
Winter L., Veilleux S., McKernan B., Kallman T., 2012, ApJ, 745, 107

APPENDIX A: INDIVIDUAL FITS FOR ACTIVE AND INACTIVE GALAXIES

Specific fits to the Ca II triplet lines for one spectrum of each of the active and inactive galaxies are shown in Fig. A1. The respective spectral segments for NGC 1365 and NGC 5506 are shown without fits, because the absorption lines could not be convincingly identified as separate features. In all cases, a single Gaussian fits the line profile very well, with no evidence for additional narrow components that might indicate a contribution from the ISM.

Specific fits to the [S II] doublet for one spectrum of each of both the active and inactive galaxies are shown in Fig. A4. The fitting process is described in Section 2.4. Equivalent fits to the [O III] doublet for the active galaxies are shown in Fig. A5. These have been fitted in the same way as the [S II] doublet, but independently, because the [S II] and [O III] profiles are not a good match to each other.

For the eight active galaxies in which we fit the auroral and transauroral lines, the fits to the strong [S II] doublet are repeated in the left-hand panels of Figs A6 and A7. The remaining three panels in each row of these figures show fits to the other lines used to estimate the electron density in the auroral/transauroral method. The line profiles have been constrained in a similar way to the [S II] doublet, with the additional criterion that only the scaling of each component is allowed to vary (the velocity offset and width are fixed to that derived from the [S II] doublet fit). Especially for the weaker lines, fitting and subtracting the continuum to minimize the impact of stellar absorption features is an important preparatory step. This has been done by fitting theoretical stellar templates to line-free regions over a wider baseline than shown in the panels, as described in Section 2.3, and checked by eye. Locations where additional line emission is expected have been marked in the various panels.

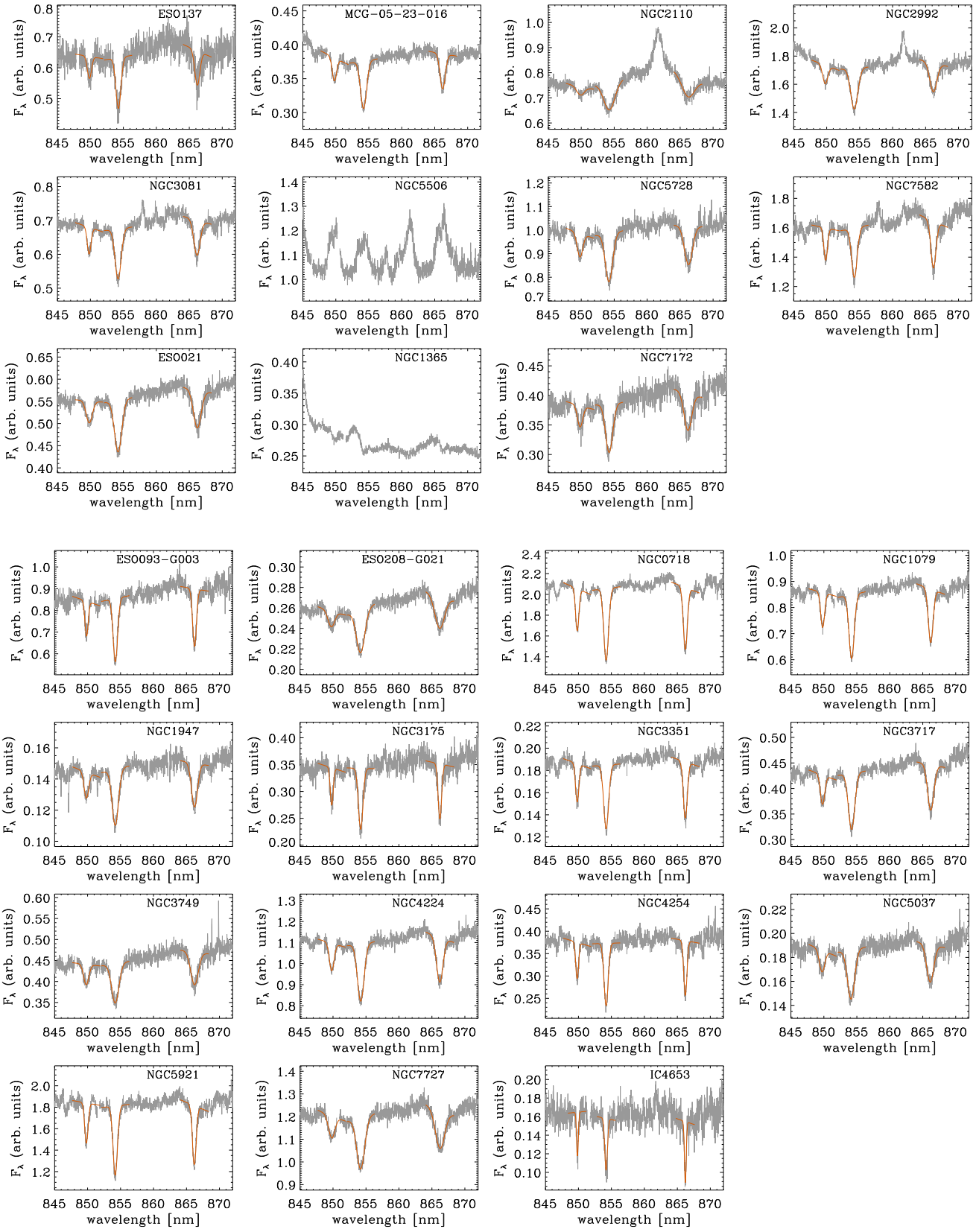

Figure A1. Fits to the Ca II triplet lines for one spectrum of each active galaxy (upper 11 panels) and inactive galaxy (lower 15 panels). Only the data are shown for NGC 1365 and NGC 5506 because there were no clear absorption lines to fit. The data are shown in grey and the fits in red. A Gaussian line profile was fitted independently to each line in order to avoid bias due to the continuum shape and emission lines. The arbitrary units of F_λ are the same for all panels.

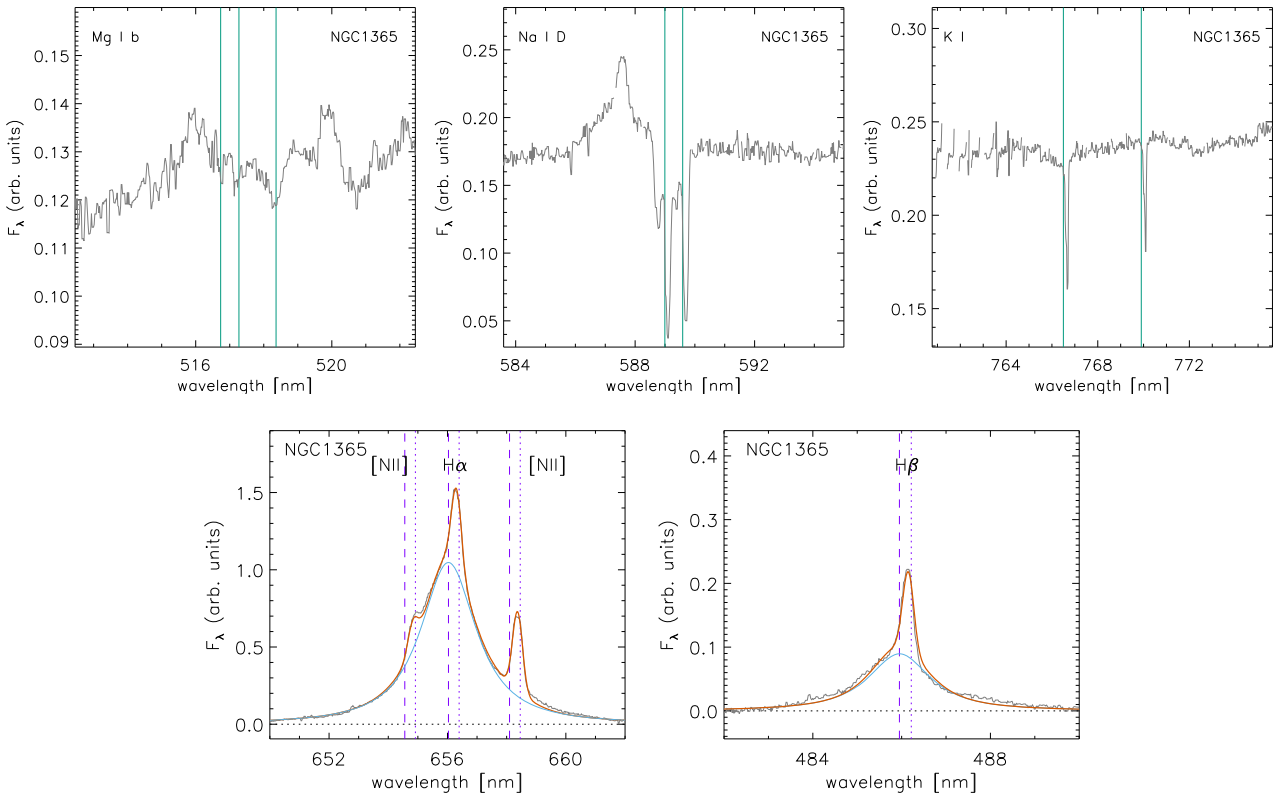

Figure A2. Spectral segments and fits to features for NGC 1365, the most complex of our AGN to fit. The arbitrary units of F_λ are the same for all panels. Top row: segments around the Mg I b triplet, the Na I D doublet, and the K I resonance doublet. The vertical green lines denote the adopted systemic velocity for each line. These are consistent with the Mg I lines, which trace stellar absorption, but show that in this object the Na I D and K I are tracing only the ISM. The Na I D shows weaker blueshifted absorption and stronger redshifted absorption, while the K I lines show only the redshifted component. Redshifted absorption tracing outflow is possible for the receding bicone projected against an extended stellar continuum. Bottom row: segments around the Hα and Hβ lines, showing the fits to the broad and narrow lines. The dashed and dotted purple lines indicate the velocities associated with the two components of Na I D absorption. The broad line has been fit with a Moffat function, centred at -110 km s^{-1} with respect to systemic, which matches the blueshifted absorption. The narrow lines are clearly offset and appear to be more associated with the redshifted absorption.

The profiles of the Hβ, [S II], and [O III] lines for the inactive galaxies are shown in Fig. A8. These show a remarkable variety of shapes, although the profiles tend to be centred close to the systemic velocity and asymmetries are less pronounced than for the active galaxies. Although there are a variety of line widths among the objects, they appear to be consistent with the gravitational potential, as indicated by the FWHM of the stellar absorption features, which is denoted by the shaded grey region.

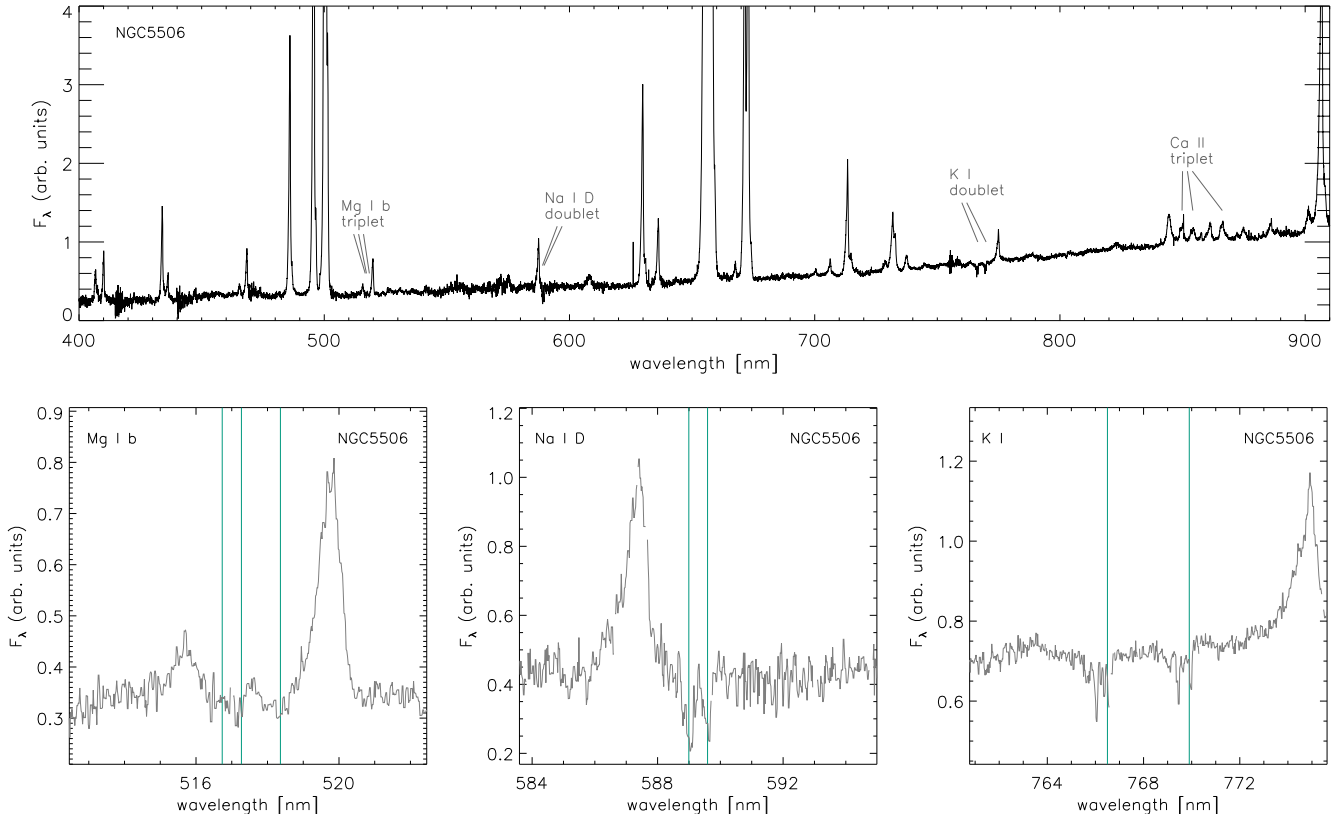

Figure A3. Spectral segments for NGC 5506.The arbitrary units of F_λ are the same for all panels. Top panel: there are very few absorption features measurable in the range 400–900 nm. The most prominent are the Na I D and K I doublets, which are dominated by the ISM. The location of the Mg I b and Ca II triplets, which would trace the stellar kinematics, is also indicated. Bottom row: panels plot the Mg I triplet, showing it is barely measurable but plausibly at our adopted systemic velocity; as well as the Na I and K I doublets, showing that they are dominated by various components of ISM absorption at a range of velocities, mostly blueshifted. The Ca II triplet region (shown in Fig. A1) is filled with line emission. In all panels, the solid green lines indicate the wavelengths of the features for our adopted systemic velocity.

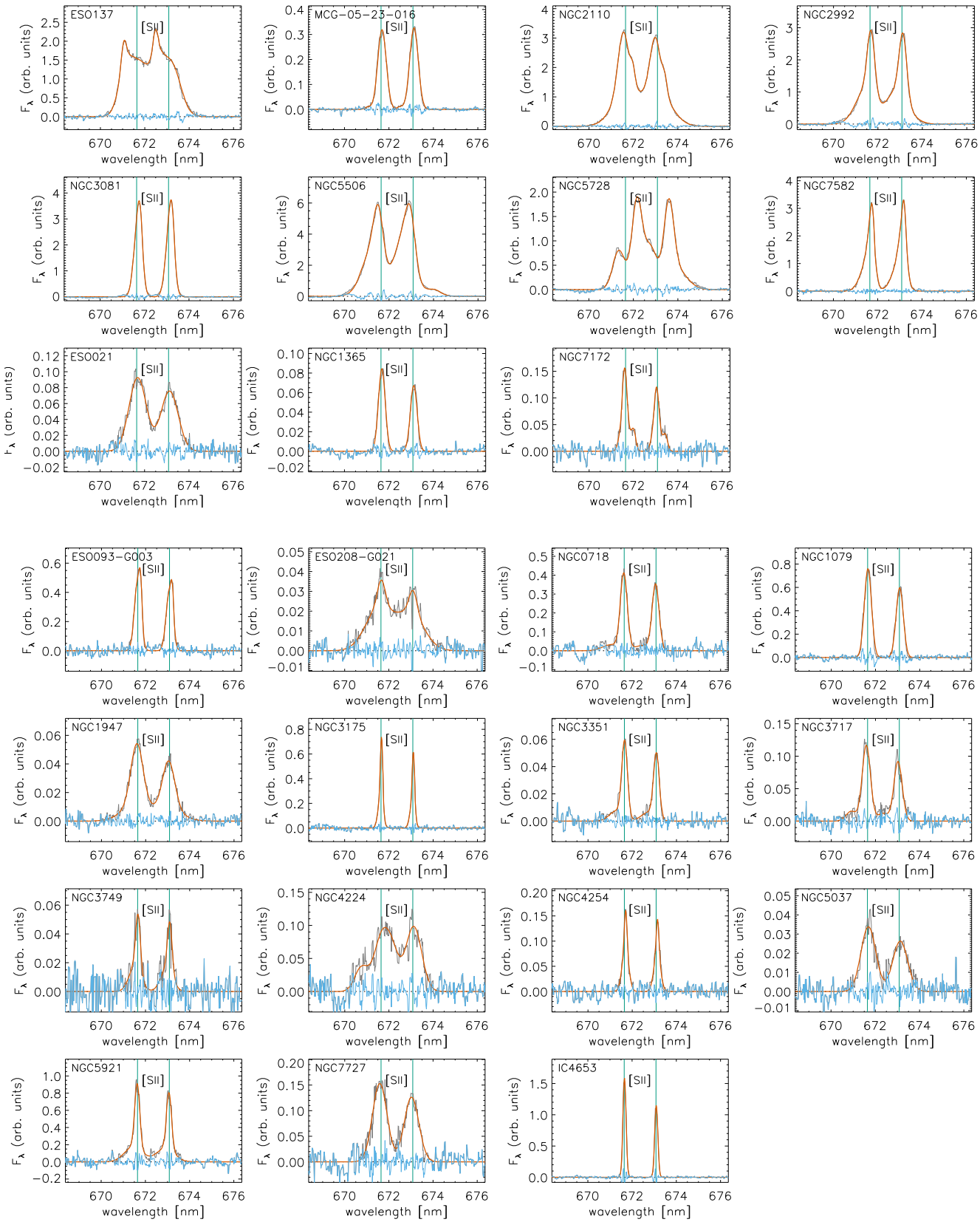

Figure A4. Fits to the [S II] doublet in one spectrum for each active galaxy (upper 11 panels) and inactive galaxy (lower 15 panels). The data are shown in grey, the fits in red, and the residuals in blue. In these plots, the fitting process included a linear function to match the local continuum. The arbitrary units of F_λ are the same for all panels.

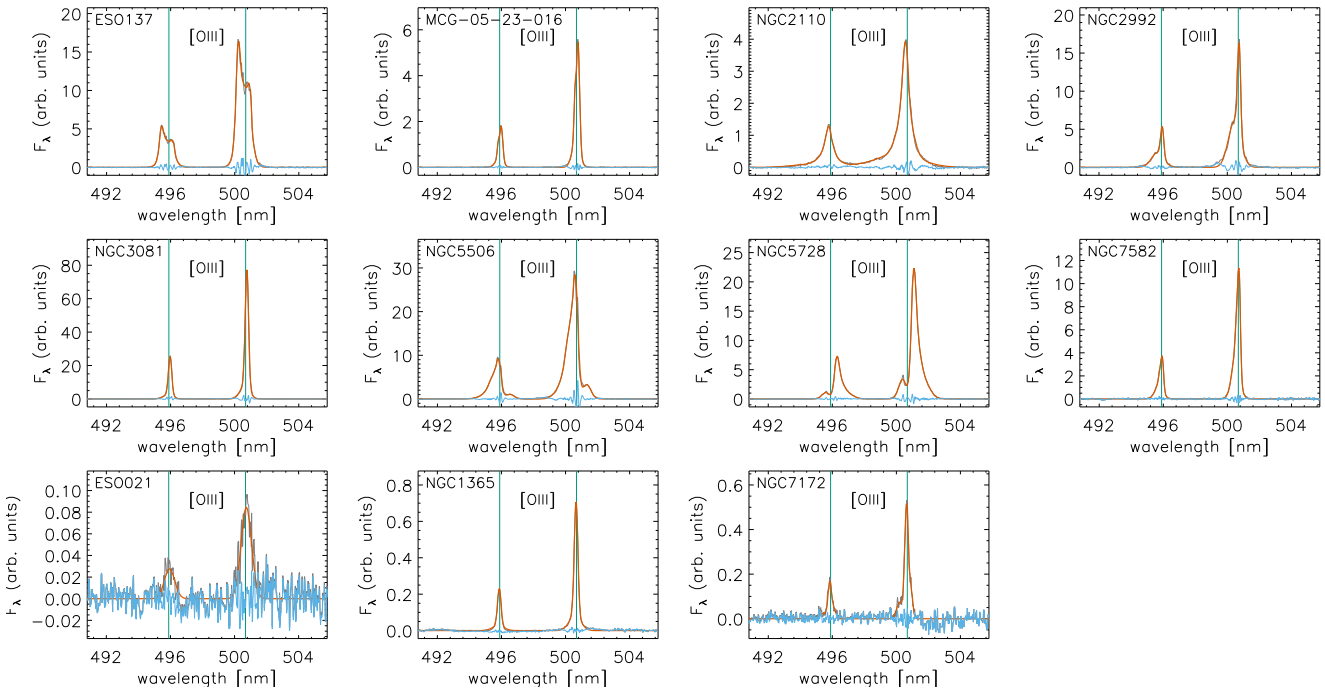

Figure A5. Fits to the [O III] doublet in one spectrum for each active galaxy. The data are shown in grey, the fits in red, and the residuals in blue. In these plots, the fitting process included a linear function to match the local continuum. The arbitrary units of F_λ are the same for all panels.

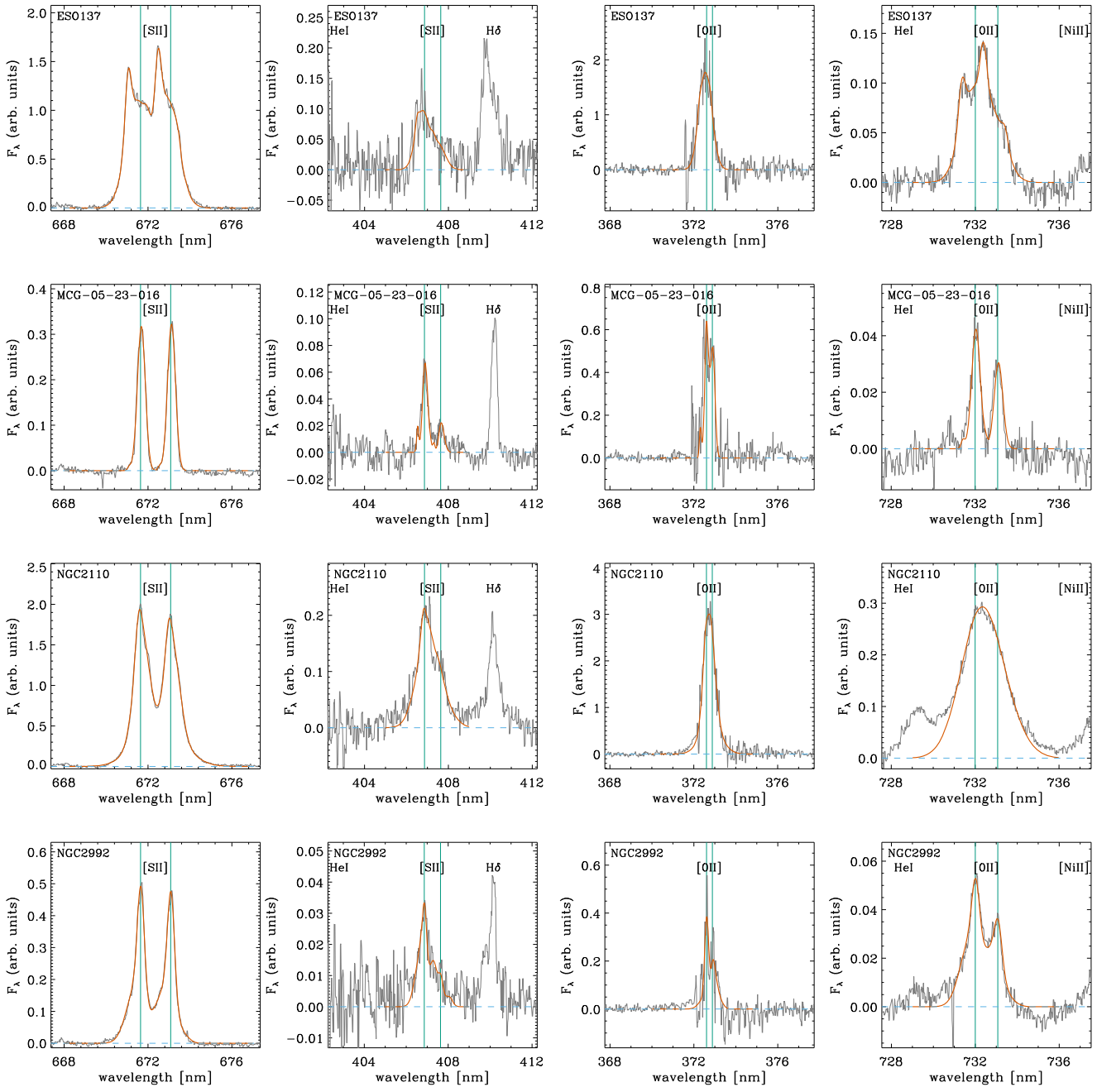

Figure A6. Fits of the various [S II] and [O II] doublets in one spectrum for each active galaxy. In these plots, a linear function to match the local continuum was fitted separately to the emission lines using line-free regions either side of the line of interest. The arbitrary units of F_λ are the same for all panels.

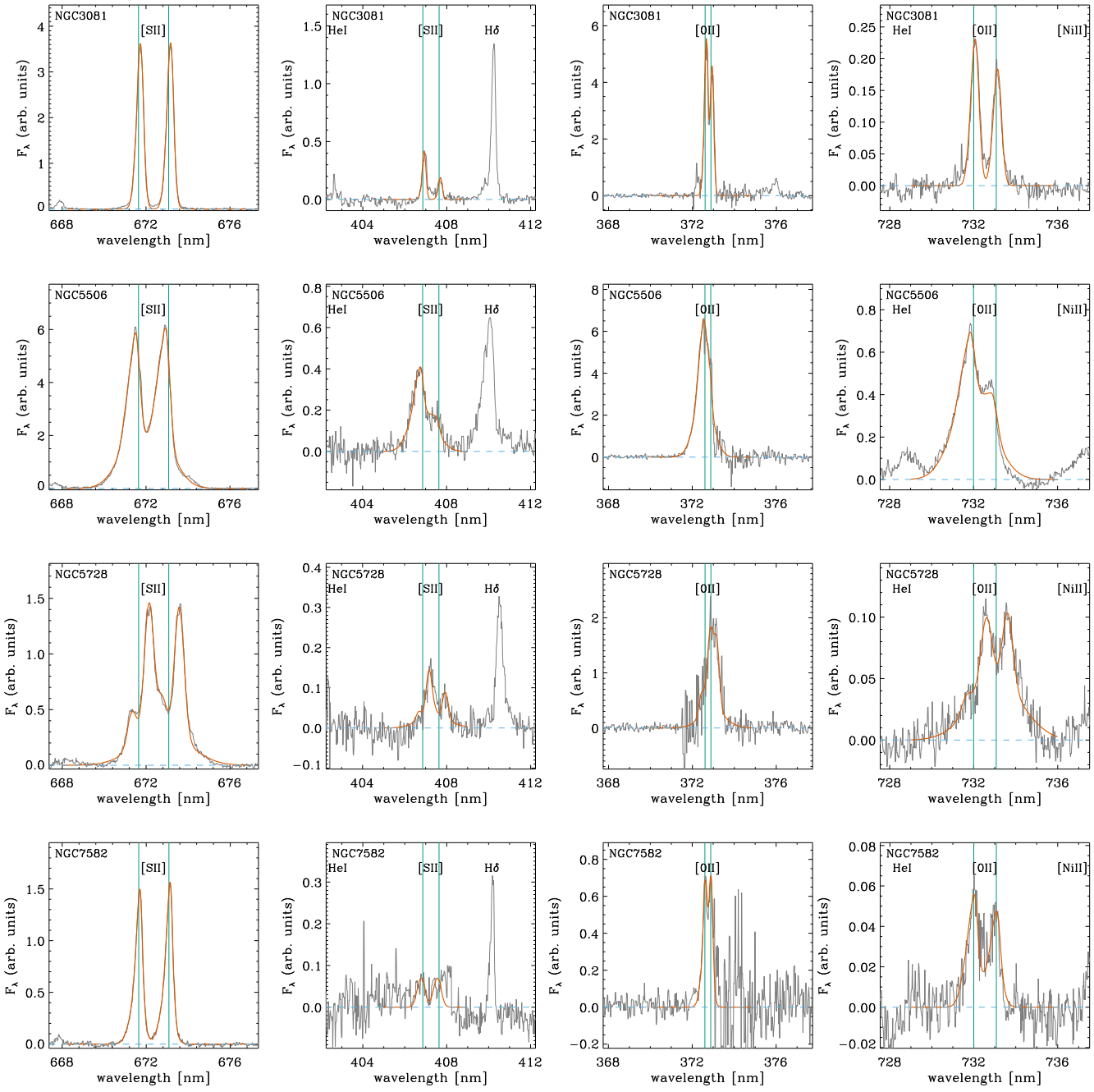

Figure A7. Fits of the various [S II] and [O II] doublets in one spectrum for each active galaxy. In these plots, a linear function to match the local continuum was fitted separately to the emission lines using line-free regions either side of the line of interest. The arbitrary units of F_λ are the same for all panels.

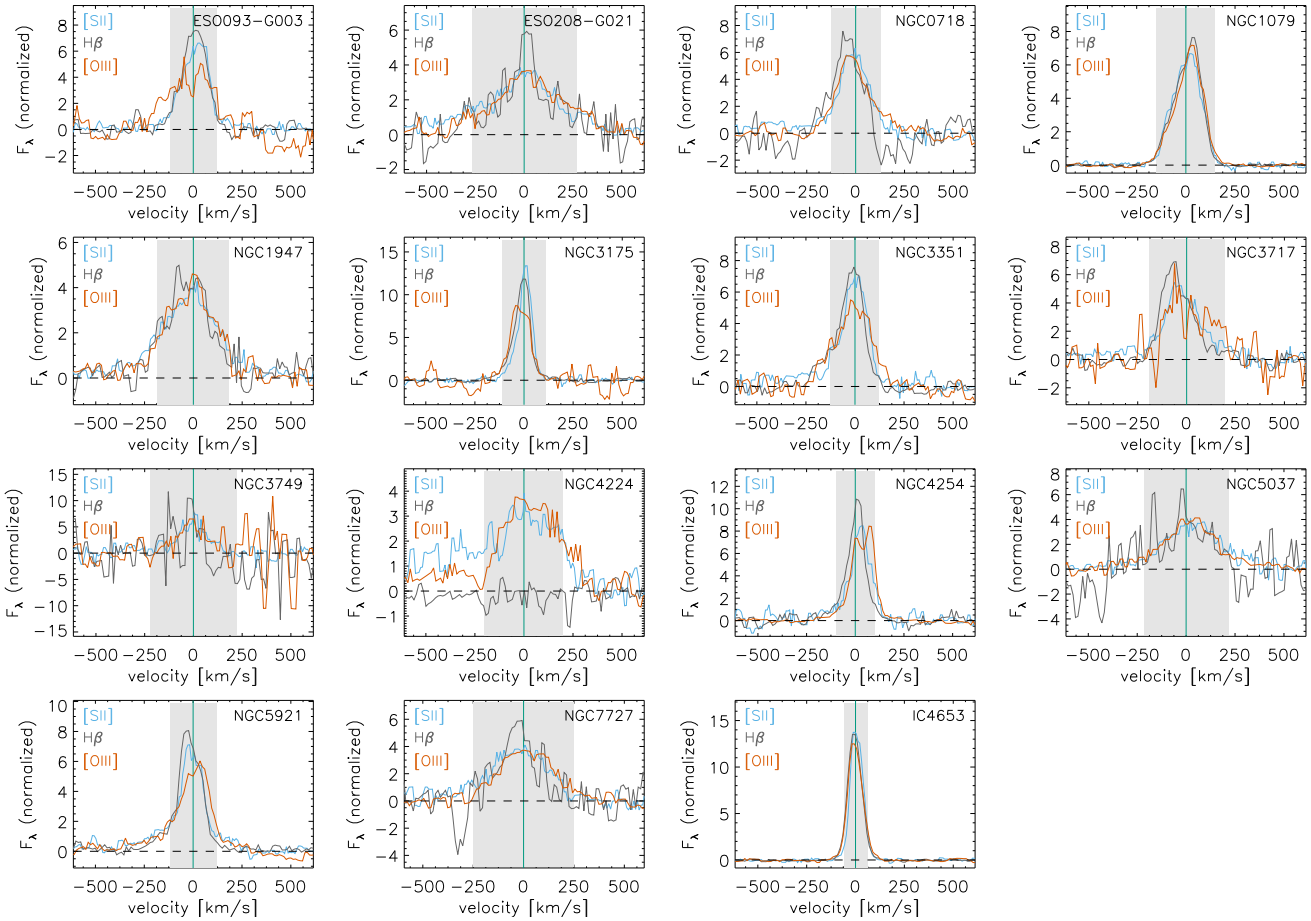

Figure A8. Comparison of the central part of the line profiles of the inactive galaxies as a function of velocity, normalized so that they have the same flux within ±250 km s^{-1}. The Hβ, [O III], and [S II] profiles (data only) are shown in grey, red, and blue, respectively; with the FWHM of the stellar absorption profile indicated by the shaded grey region for reference. For visualization purposes, the [S II] profile is a combination of the short side of the 6716 Å line and the long side of the 6731 Å line, scaled to match where they overlap.

This paper has been typeset from a TEX/LATEX file prepared by the author.